A two-dimensional modal method for spatial rehomogenization of nodal cross sections and discontinuity-factor correction

Gamarino, Matteo; Dall'Osso, Aldo; Lathouwers, Danny; Kloosterman, Jan Leen

DOI
10.1016/j.anucene.2018.10.012

Publication date
2019

Document Version
Final published version

Published in
Annals of Nuclear Energy

Citation (APA)
Gamarino, M., Dall'Osso, A., Lathouwers, D., & Kloosterman, J. L. (2019). A two-dimensional modal method for spatial rehomogenization of nodal cross sections and discontinuity-factor correction. *Annals of Nuclear Energy*, *125*, 157-185. https://doi.org/10.1016/j.anucene.2018.10.012

Annals of Nuclear Energy 125 (2019) 157–185

Contents lists available at ScienceDirect

Annals of Nuclear Energy

journal homepage: www.elsevier.com/locate/anucene

A two-dimensional modal method for spatial rehomogenization of nodal cross sections and discontinuity-factor correction

Matteo Gamarino [a,*], Aldo Dall'Osso [b], Danny Lathouwers [a], Jan Leen Kloosterman [a]

[a] Delft University of Technology, Department of Radiation, Science and Technology, Mekelweg 15, 2629 JB Delft, The Netherlands
[b] Framatome Tour AREVA, 92084 Paris La Défense Cedex, France

ARTICLE INFO

Article history:
Received 12 August 2018
Received in revised form 29 September 2018
Accepted 3 October 2018

Keywords:
Nodal methods
Homogenization
Spatial effects
Transverse leakage
Pin-power reconstruction

ABSTRACT

We propose a two-dimensional (2-D) modal approach for spatial rehomogenization of nodal cross sections in light water reactor analysis. This algorithm aims to synthesize the variation in the 2-D intranodal distributions of the few-group flux and directional net currents between the core environment and the infinite-lattice approximation. Assembly discontinuity factors are also corrected. The method is validated on a broad set of pressurized-water-reactor benchmark problems. Its accuracy is assessed on both nodal quantities and the reconstructed pin-by-pin flux and power distributions. We show that the errors in the effective multiplication factor and assembly-averaged fission power significantly decrease compared to the calculation with infinite-medium homogenization parameters. In most cases, an improvement is also found at the pin level. A thorough discussion follows, which addresses the use of the 2-D neutron current information to compute the transverse-leakage distribution for the transverse-integrated nodal equations, the potential dual application of the method for rehomogenization and dehomogenization, and the quantification of the contributions of various environmental effects (spatial, spectral, and cross energy-space) to homogenization errors.

1. Introduction

The accuracy of two-group, coarse-mesh nodal diffusion calculations is hindered by spatial homogenization and energy condensation errors in the infinite-medium cross sections and discontinuity factors (Smith, 1994; Palmtag and Smith, 1998). This aspect is a major drawback of the conventional two-step procedure, which combines off-line single-assembly heterogeneous transport calculations with the on-line simulation of the assembly-homogenized core representation (Smith, 1986; Sanchez, 2009). In previous work (Gamarino et al., 2018a; Gamarino et al., 2018b), spectral rehomogenization was applied successfully to improve the accuracy of nodal cross sections by computing the variation in the neutron flux spectrum between the core environment and the infinite-lattice approximation. In this paper, we aim to correct the spatial component of single-assembly cross-section defects.

Spatial homogenization errors are significant when highly absorbing elements (such as control rods and burnable-poison rods) are located at the assembly periphery, thus experiencing steep flux gradients, as well as in the presence of strongly heterogeneous fuel composition (such as in MOX assemblies). Several methods have been proposed to incorporate spatial effects into the nodal cross sections. Spatial heterogeneity due to non-uniform intranodal depletion (i.e., gradients in the burn-up and nuclide concentrations) and fuel temperature is commonly modeled with a separable (along each coordinate axis) quadratic expansion of the nodal cross sections (Wagner et al., 1981; Forslund et al., 2001). A similar approach has been applied to represent design heterogeneity (Shatilla et al., 1996). However, these methods do not correct the spatial homogenization error due to deviations in the flux distribution between the environment and the infinite lattice. One of the first spatial rehomogenization techniques was proposed by Smith (1994). In his approach, the transverse-integrated intranodal cross sections are spatially (re) homogenized at each power iteration or thermal-feedback update with the computed one-dimensional (1-D) heterogeneous flux shape. This shape is obtained via superposition of the heterogeneous infinite-lattice transverse-integrated flux form function and the homogeneous flux distribution from the transverse-integrated nodal calculation. This method uses single-assembly-generated rehomogenization coefficients and can be easily incorporated into existing codes. However, it does not correct the assembly discontinuity factors. A variant of it was later proposed by Palmtag (1997). In Dall'Osso (2014), the variation in the 1-D

* Corresponding author.
E-mail address: matteo.gamarino@gmail.com (M. Gamarino).

https://doi.org/10.1016/j.anucene.2018.10.012
0306-4549/

transverse-integrated flux between the real environment and the infinite lattice is evaluated with a modal expansion. This approach also corrects the discontinuity factors.

Another method for spatial rehomogenization is the 2-D submesh model that has been implemented in Studsvik's nodal code SIMULATE (Bahadir et al., 2005; Bahadir and Lindahl, 2009). In this strategy, each radial node (i.e., fuel assembly or assembly quarter) is subdivided into $N \times N$ homogeneous rectangular subnodes (typically with N = 5). The 2-D diffusion equation is solved in every subregion with the corresponding infinite-medium homogenization parameters. The axial leakage (known from the global 3-D solution) is converted into an equivalent absorption cross section. The resulting intranodal flux distribution is used to rehomogenize the single-assembly cross sections over the submeshes and to estimate the environmental discontinuity factors at the assembly outer edges. The 2-D submesh calculation is combined with an axial homogenization model to handle axial heterogeneity.

Radial zoning of fuel-assembly homogenization can also be used to reduce spatial errors. For example, EDF's core simulator COCAGNE (Guillo et al., 2017) features a discretization of 2×2 subregions in each assembly quarter. Non-uniform nodes are used to model separately (*i*) the four fuel pins in every external corner of the assembly, (*ii*) the outer and first inboard pin rows (at the assembly periphery), and (*iii*) the remainder of the fuel bundle. This meshing strategy has been chosen to minimize the level of heterogeneity in each subregion that is homogenized. In spite of their enhanced accuracy, refined-mesh approaches entail a somewhat higher computational effort than conventional nodal methods, which only use one or four nodes per fuel assembly.

Other methods do not specifically focus on spatial effects and try to model the global environmental effect. For example, in Rahnema and Nichita (1997), the corrections on the nodal cross sections and discontinuity factors are tabulated in the standard parameterized libraries versus the current-to-flux ratio (or other albedo parameters) at the node surfaces. These corrections are computed during the lattice calculation via parametric assembly simulations with varying albedo boundary conditions. They are interpolated during the nodal calculation just as the infinite-lattice group constants. Recently, a variant of this approach has been investigated (Kim et al., 2017). The drawback of this kind of method is that it demands multiple single-assembly calculations for each lattice state. Rahnema et al. (2002) developed high-order cross-section homogenization, which does not require additional lattice simulations. Using high-order boundary-condition perturbation theory (McKinley and Rahnema, 2000), the environmental homogenization parameters are expanded in terms of the surface current-to-flux ratio. The expansion coefficients are evaluated using the known unperturbed solution of the zero-leakage problem. This method requires two infinite-medium adjoint functions, which are precomputed and stored as additional parameters in the cross-section tables. Clarno and Adams (2005) proposed to capture neighbor effects during the single-assembly calculation via spatial superposition of typical four-assembly configurations. Recently, Groenewald et al. (2017) developed a semi-heterogeneous transport-embedded approach, in which the embedded transport calculations are performed with a simplified handling of spatial heterogeneity, energy discretization and solution operator. The computational burden of transport-nodal iterations is thus mitigated.

In this paper, we propose an extension of the spatial rehomogenization technique described in Dall'Osso (2014). This method aims to compute on the fly the change in the intranodal flux shape that is used for cross-section spatial homogenization when the assembly is in the core environment. The rehomogenization problem is solved locally (namely, independently in each node) after each power iteration, using as boundary conditions the estimates of the volume-averaged fluxes, the surface-averaged fluxes and currents, and the multiplication factor from the global (i.e., core-wide) nodal calculation. Only radial heterogeneity is addressed. The effect of axial heterogeneity is taken into account via axial homogenization or control-rod cusping models (Dall'Osso, 2002). Two significant approximations are made in the formulation presented in Dall'Osso (2014):

- The 2-D rehomogenization problem is simplified via transverse integration into two 1-D problems, which are solved sequentially in the x and y directions.
- The transverse-integrated fine-mesh cross sections (to be weighted with the computed 1-D flux change) are obtained by collapsing the 2-D pin-by-pin cross-section distributions with the infinite-medium flux form function, instead of the environmental flux shape.

In this work, the above assumptions are relaxed by developing a full 2-D rehomogenization model, which retains the non-separability of the flux variation in the x and y directions. In this way, the 2-D distributions of the environmental flux and directional net currents can be estimated at the nodal flux iteration level. Moving to a 2-D model is also motivated by the possibility to use the so obtained 2-D information (*i*) to compute the transverse-leakage distributions for the transverse-integrated nodal equations, and (*ii*) to reconstruct the pin-by-pin flux and power distributions directly (i.e., without the dehomogenization phase).

This paper is structured as follows. The 2-D rehomogenization method is described in Section 2. Section 3 shows the numerical results of several Pressurized-Water-Reactor (PWR) multiassembly configurations, in which the spatial effects of the environment are important. The accuracy of the method is assessed on both nodal and pin-by-pin quantities. A comparison with the simplified 1-D approach is made. In Section 4, we discuss various aspects of interest of spatial rehomogenization. These include the correction of assembly discontinuity factors, the calculation of the transverse-leakage shape with the information from the 2-D rehomogenization, and the contributions of various environmental effects (spatial, spectral, and mixed energy-space) to the deviations of nodal cross sections from the single-assembly values. Concluding remarks follow in Section 5.

2. Description of the method

We introduce a non-dimensional coordinate u_d, where d stands for x or y. The following change of variable is applied:

$$d, \quad d \in [0, \Delta d] \quad \rightarrow \quad u_d = \frac{d}{\Delta d} - \frac{1}{2}, \quad u_d \in \left[-\frac{1}{2}, \frac{1}{2}\right]. \tag{1}$$

We define the 2-D intranodal distribution of the environmental neutron flux density in the coarse energy group G as

$$\Phi_{\mathrm{env},G}(u_x, u_y) = \bar{\Phi}_G \varphi_{\infty,G}(u_x, u_y) + \delta\Phi_G(u_x, u_y), \tag{2}$$

where $\bar{\Phi}_G$ is the volume-averaged flux from the nodal calculation, $\varphi_{\infty,G}(u_x, u_y)$ is the infinite-medium flux distribution (normalized to unity) used for cross-section spatial homogenization in the lattice calculation, and $\delta\Phi_G(u_x, u_y)$ is the flux spatial variation between the environmental and infinite-medium conditions. The distributions $\Phi_{\mathrm{env},G}(u_x, u_y)$ and $\varphi_{\infty,G}(u_x, u_y)$ are heterogeneous quantities, whereas $\delta\Phi_G(u_x, u_y)$ is assumed to be a smoothly varying function. The node-averaged value of $\delta\Phi_G(u_x, u_y)$ is zero to satisfy the normalization condition

$$\int_{-1/2}^{1/2} du_x \int_{-1/2}^{1/2} du_y \Phi_{\mathrm{env},G}(u_x,u_y) = \bar{\Phi}_G. \tag{3}$$

The flux change is approximated with a 2-D modal expansion:

$$\delta\Phi_G(u_x,u_y) = \sum_{i_x=1}^{N_x} \alpha_{G,x,i_x} P_{G,i_x}(u_x) + \sum_{i_y=1}^{N_y} \alpha_{G,y,i_y} P_{G,i_y}(u_y) + \sum_{\substack{c_x=1 \\ c_x+c_y\leqslant N_c}}^{N_x} \sum_{c_y=1}^{N_y} \alpha_{G,xy,c_x,c_y} P_{G,c_x}(u_x) P_{G,c_y}(u_y). \tag{4}$$

The non-separability of the flux variation is modeled with the cross terms α_{G,xy,c_x,c_y}. In this work, for each coarse group we consider directional expansions with four basis functions (i.e., $N_x = N_y = N = 4$) and we retain four cross terms ($N_{\mathrm{cross}} = 4$). The basis functions $P_{G,i_d}(u_d)$ are the conventional polynomial and hyperbolic functions used for the 1-D transverse-integrated flux expansion in the semi-analytic Nodal Expansion Method (NEM), with the only exception of $P_{2,4}(u_d)$:

$$P_{G,1}(u_d) = u_d \quad (G = 1,2); \tag{5a}$$

$$P_{G,2}(u_d) = u_d^2 - \frac{1}{12} \quad (G = 1,2); \tag{5b}$$

$$P_{1,3}(u_d) = u_d\left(u_d^2 - \frac{1}{4}\right), \quad P_{2,3}(u_d) = sinh(\eta u_d); \tag{5c}$$

$$P_{1,4}(u_d) = \left(u_d^2 - \frac{1}{4}\right)\left(u_d^2 - \frac{1}{20}\right),$$
$$P_{2,4}(u_d) = cosh(\eta u_d) - \frac{2}{\eta} sinh\left(\frac{\eta}{2}\right). \tag{5d}$$

In Eqs. (5c) and (5d), the coefficient η is chosen so that the hyperbolic functions $sinh(\eta u_d)$ and $cosh(\eta u_d)$ are particular solutions of the 1-D homogeneous diffusion equation in the thermal group:

$$\eta = \Delta d \sqrt{\frac{\Sigma_{a,2} + \sum_{G'=1}^{2} \Sigma_{s,2\to G'}}{D_2}}. \tag{6}$$

The basis functions of Eq. (5) proved to accurately reconstruct the 1-D transverse-integrated flux variation (Dall'Osso, 2014) and have been also used in this work for their generality. The above modes have zero average value in the interval $[-1/2, 1/2]$, thus satisfying Eq. (3). The four cross terms in Eq. (4) only have polynomial components, with global order up to 4 (i.e., N_c = 4) and directional order up to 2.

The spatial distribution of the directional net neutron current $J_{\mathrm{env},G,d}(u_x,u_y)$ is defined as

$$J_{\mathrm{env},G,d}(u_x,u_y) = \bar{\Phi}_G J_{\infty,G,d}(u_x,u_y) + \delta J_{G,d}(u_x,u_y), \tag{7}$$

with

$$\delta J_{G,d}(u_x,u_y) = -\frac{D_G(u_x,u_y)}{\Delta d} \frac{\partial}{\partial u_d} \delta\Phi_G(u_x,u_y). \tag{8}$$

In Eq. (7), scaling to the volume-averaged flux $\bar{\Phi}_G$ ensues from the application of Fick's law to Eq. (2). In Eq. (8), $D_G(u_x,u_y)$ is the spatially dependent diffusion coefficient (in units of cm). We define the environmental discontinuity factors $f^{\mathrm{env}}_{G,d\pm}$ at the node surfaces as

$$f^{\mathrm{env}}_{G,d\pm} = f^{\infty}_{G,d\pm} + \delta f_{G,d\pm}, \tag{9}$$

where $f^{\infty}_{G,d\pm}$ denotes the single-assembly discontinuity factor, and the signs $\pm$ refer to the interfaces along the positive and negative directions of the d axis.

The following nodal unknowns must be found for each coarse group [Eqs. (4) and (9)]: the directional modal coefficients α_{G,d,i_d} (4 unknowns per direction), the cross modal coefficients α_{G,xy,c_x,c_y} (4 unknowns), and the discontinuity-factor corrections $\delta f_{G,d\pm}$ (2 unknowns per direction). With the aforementioned choice of N and N_c, the number of unknowns per coarse group is 16. In order to solve for them, we identify a set of equations for the following quantities:

- the environmental surface-averaged fluxes (2 equations per direction, per group);
- the environmental surface-averaged net currents (2 equations per direction, per group);
- the environmental corner-point fluxes (4 equations per group).

The remaining four (or $[(N_x + N_y + N_{\mathrm{cross}}) - 8]$ in a more general framework) equations per group are found applying a standard weighted-residual technique to the 2-D few-group balance equation in the environmental conditions. The procedure used to derive the aforementioned equations is explained below.

2.1. Equations for the environmental surface-averaged flux

The surface-averaged heterogeneous (i.e., continuous) flux in the environmental conditions $\Phi^{\mathrm{het}}_{G,d\pm}$ can be written, for the x direction, as

$$\Phi^{\mathrm{het}}_{G,x\pm} = \int_{-1/2}^{1/2} du_y \Phi_{\mathrm{env},G}(u_x,u_y)|_{u_x=\pm\frac{1}{2}} = f^{\mathrm{env}}_{G,d\pm} \Phi^{\mathrm{hom}}_{G,x\pm}, \tag{10}$$

where $\Phi^{\mathrm{hom}}_{G,x\pm}$ denotes the homogeneous (i.e., discontinuous) surface-averaged flux from the nodal calculation. Introducing Eqs. (2) and (9) into Eq. (10) yields

$$\bar{\Phi}_G \int_{-1/2}^{1/2} du_y \varphi_{\infty,G}(u_x,u_y)|_{u_x=\pm\frac{1}{2}} + \int_{-1/2}^{1/2} du_y \delta\Phi_G(u_x,u_y)|_{u_x=\pm\frac{1}{2}} = \left(f^{\infty}_{G,x\pm} + \delta f_{G,x\pm}\right)\Phi^{\mathrm{hom}}_{G,x\pm}. \tag{11}$$

Using the definition of single-assembly discontinuity factor and taking into account that the volume-averaged value of $\varphi_{\infty,G}(u_x,u_y)$ is unity, we rewrite the first term on the left-hand side of Eq. (11) as

$$\bar{\Phi}_G \int_{-1/2}^{1/2} du_y \varphi_{\infty,G}(u_x,u_y)|_{u_x=\pm\frac{1}{2}} = \bar{\Phi}_G f^{\infty}_{G,x\pm}. \tag{12}$$

After substituting Eqs. (4) and (12) into Eq. (11), we obtain

$$\sum_{i_x=1}^{N_x} \alpha_{G,x,i_x} P_{G,i_x}\left(\pm\frac{1}{2}\right) = \left(f^{\infty}_{G,x\pm} + \delta f_{G,x\pm}\right)\Phi^{\mathrm{hom}}_{G,x\pm} - f^{\infty}_{G,x\pm}\bar{\Phi}_G. \tag{13}$$

In Eq. (13), the transverse-direction (i.e., y-directional) and cross components of the surface-averaged flux variation vanish because, by definition,

$$\int_{-1/2}^{1/2} du_y P_{G,i_y}(u_y) = 0. \tag{14}$$

An equation analogous to Eq. (13) holds for the y direction.

2.2. Equations for the environmental surface-averaged current

We consider the simple case with homogeneous diffusion coefficient [i.e., $D_G(u_x,u_y) = D_G$]. Using Eqs. (7) and (8), the surface-averaged directional net current reads (for the x axis)

$$\int_{-1/2}^{1/2} du_y J_{\mathrm{env},G,x}(u_x,u_y)|_{u_x=\pm\frac{1}{2}} = -\frac{D_G}{\Delta x}\int_{-1/2}^{1/2} du_y \frac{\partial}{\partial u_x}\delta\Phi_G(u_x,u_y)|_{u_x=\pm\frac{1}{2}} = -\frac{D_G}{\Delta x}\left[\sum_{i_x=1}^{N_x}\alpha_{G,x,i_x}\frac{dP_{G,i_x}}{du_x}(u_x)|_{u_x=\pm\frac{1}{2}}\right]. \quad (15)$$

In Eq. (15), we have used the fact that the infinite-medium current at the assembly surface is zero, namely

$$J_{\infty,G,x}(u_x,u_y)|_{u_x=\pm\frac{1}{2}} = 0. \quad (16)$$

Eq. (16) is valid at the assembly outer edges and, when considering four nodes per fuel assembly, at the internal surfaces of fully symmetrically-loaded fuel bundles (i.e., with octant or quadrant symmetry).

The sought equation is found equating Eq. (15) to the surface-averaged directional net current $J_{G,x\pm}$ from the nodal calculation:

$$-\frac{D_G}{\Delta x}\left[\sum_{i_x=1}^{N_x}\alpha_{G,x,i_x}\frac{dP_{G,i_x}}{du_x}(u_x)|_{u_x=\pm\frac{1}{2}}\right] = J_{G,x\pm}. \quad (17)$$

2.3. Equations for the environmental corner-point flux

The heterogeneous (i.e., continuous) flux at a nodal corner point is

$$\Phi_{G,c}^{\mathrm{het}} = \Phi_{\mathrm{env},G}(u_x,u_y)|_{\substack{u_x=u_x^c\\u_y=u_y^c}} = \bar{\Phi}_G\varphi_{\infty,G}(u_x,u_y)|_{\substack{u_x=u_x^c\\u_y=u_y^c}} + \delta\Phi_G(u_x,u_y)|_{\substack{u_x=u_x^c\\u_y=u_y^c}}, \quad (18)$$

where u_x^c and u_y^c denote the corner-point coordinates within the node. Introducing the single-assembly corner discontinuity factor $f_{G,c}^{\infty}$ and substituting Eq. (4), Eq. (18) becomes

$$\sum_{i_x=1}^{N_x}\alpha_{G,x,i_x}P_{G,i_x}(u_x^c) + \sum_{i_y=1}^{N_y}\alpha_{G,y,i_y}P_{G,i_y}(u_y^c) + \sum_{\substack{c_x=1\\c_x+c_y\leqslant N_c}}^{N_x}\sum_{c_y=1}^{N_y}\alpha_{G,xy,c_x,c_y}P_{G,c_x}(u_x^c)P_{G,c_y}(u_y^c) = \Phi_{G,c}^{\mathrm{het}} - \bar{\Phi}_G f_{G,c}^{\infty}. \quad (19)$$

An estimate of $\Phi_{G,c}^{\mathrm{het}}$ must be found to use Eq. (19) in the spatial rehomogenization algorithm. For this purpose, we use two different approaches:

- a combination of Smith's method (Rempe et al., 1989) and the Method of Successive Smoothing (MSS) (Böer and Finnemann, 1992);
- a Corner Point Balance (CPB) condition (Chang et al., 1989).

The above methods are commonly used in the context of fuel-assembly dehomogenization (Joo et al., 2009). Their application in the framework of our work is briefly explained in the following.

2.3.1. Smith's method and the Method of Successive Smoothing

In Smith's method, the intranodal flux distribution is considered as separable in the x and y directions. The homogeneous flux at a given node vertex is approximated using the volume-averaged flux in the node and the surface-averaged flux at the nodal edges crossing the corner. For instance, using the nodal coordinate system of Fig. 1, the flux in the north-east corner $\Phi_{G,NE}^{\mathrm{hom}}$ reads

$$\Phi_{G,NE}^{\mathrm{hom}} = \frac{\Phi_{G,x+}^{\mathrm{hom}}\Phi_{G,y+}^{\mathrm{hom}}}{\bar{\Phi}_G}. \quad (20)$$

The MSS is based on the assumption that the flux varies linearly in the neighborhood of a corner point. The homogeneous flux at a nodal vertex is estimated with a linear extrapolation in terms of the surface-averaged and volume-averaged fluxes:

$$\Phi_{G,NE}^{\mathrm{hom}} = \Phi_{G,x+}^{\mathrm{hom}} + \Phi_{G,y+}^{\mathrm{hom}} - \bar{\Phi}_G. \quad (21)$$

The heterogeneous corner flux in the environment is related to its homogeneous counterpart $\Phi_{G,c}^{\mathrm{hom}}$ via the corner discontinuity factor:

$$\Phi_{G,c}^{\mathrm{het}} = f_{G,c}^{\mathrm{env}}\Phi_{G,c}^{\mathrm{hom}}. \quad (22)$$

Using Eqs. (20) or (21) and Eq. (22), four estimates of $\Phi_{G,c}^{\mathrm{het}}$ are available for a given corner point, one from each node surrounding the corner. The heterogeneous corner flux is thus approximated with the arithmetic average of the available estimates:

$$\Phi_{G,c}^{\mathrm{het}} = \frac{1}{4}\left(\Phi_{G,c,i,j}^{\mathrm{hom}}f_{G,c,i,j}^{\mathrm{env}} + \Phi_{G,c,i+1,j}^{\mathrm{hom}}f_{G,c,i+1,j}^{\mathrm{env}} + \Phi_{G,c,i,j+1}^{\mathrm{hom}}f_{G,c,i,j+1}^{\mathrm{env}} + \Phi_{G,c,i+1,j+1}^{\mathrm{hom}}f_{G,c,i+1,j+1}^{\mathrm{env}}\right), \quad (23)$$

where we have denoted with i and j the coordinates (along the x and y axes, respectively) of the four nodes sharing the corner c. In the real environment, the corner discontinuity factors also change compared to their infinite-lattice estimates. An environmental correction on this parameter ($\delta f_{G,c}$) should therefore be introduced for each node vertex. In order not to increase the number of unknowns and equations of the rehomogenization problem, we use an approximate relation to evaluate this correction. We assume that $\delta f_{G,c}$ is proportional to the corrections on the discontinuity factors of the x- and y-directional surfaces crossing the corner ($\delta f_{G,x}, \delta f_{G,y}$), namely

$$\frac{f_{G,c}^{\infty} + \delta f_{G,c}}{f_{G,c}^{\infty}} = \frac{f_{G,x}^{\mathrm{env}} + f_{G,y}^{\mathrm{env}}}{f_{G,x}^{\infty} + f_{G,y}^{\infty}}, \quad (24)$$

where $f_{G,x}^{\mathrm{env}}$ and $f_{G,y}^{\mathrm{env}}$ are the environmental discontinuity factors estimated with Eq. (9) at the previous rehomogenization iteration.

Previous work showed that the MSS generally performs better than Smith's method, in which spatial cross effects are neglected (F. Khoshahval et al., 2014). On the other hand, Eq. (21) may lead to a negative corner flux (especially at the first nodal iterations, when the surface-averaged flux estimates are not yet accurate enough). For this reason, we use Eq. (21) as a default option and switch to Eq. (20) in case of negative corner-flux values from the MSS. Despite the ease of implementation, this approach may fail to provide accurate estimates of the corner fluxes if the flux distribution exhibits strong spatial gradients (Rempe et al., 1989; Joo et al., 2009).

2.3.2. The Corner Point Balance approach

The Corner Point Balance (Chang et al., 1989) is a neutron balance equation imposing the absence of net source conditions at

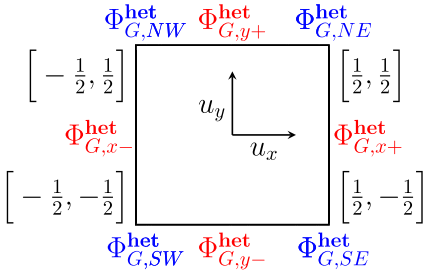

Fig. 1. Corner-point coordinate system in a generic node. The corner and surface-averaged fluxes are highlighted.

the corner points (i.e., no accumulation of neutrons within an infinitesimally small volume). With this method, continuity of the neutron current at the vertices of a node is preserved.

We briefly review this approach with an analogy to the simple case of 1-D problem (Joo et al., 2009). From diffusion theory, the heterogeneous surface-averaged flux at the interface s between two adjacents node k and l is related to the inlet ($J^{\text{in}}_{G,s}$) and outlet ($J^{\text{out}}_{G,s}$) partial currents as

$$\Phi_{G,s} = 2\left(J^{\text{in}}_{G,s} + J^{\text{out}}_{G,s}\right), \tag{25}$$

where

$$J^{\text{in}}_{G,s} = \frac{1}{4}\Phi_{G,s} + \frac{1}{2}J_{G,s}, \quad J^{\text{out}}_{G,s} = \frac{1}{4}\Phi_{G,s} - \frac{1}{2}J_{G,s}. \tag{26}$$

If no continuity of the net current $J_{G,s}$ is imposed, the estimates of $J_{G,s}$ computed for the nodes k and l will be different (i.e., $J^{k}_{G,s} \neq J^{l}_{G,s}$). Inserting Eq. (26) into Eq. (25) yields

$$\Phi^{*}_{G,s} = \Phi_{G,s} + \left(J^{k}_{G,s} - J^{l}_{G,s}\right). \tag{27}$$

Eq. (27) defines an iterative algorithm, in which a new estimate of the surface flux $\Phi^{*}_{G,s}$ is obtained from the previous one and the difference in the computed net currents, which will eventually converge to zero.

A similar scheme can be applied in the neighborhood of a corner point. As illustrated in Fig. 2, four sets of directional net currents exist at a given nodal vertex (one for each adjacent node): $J^{1}_{x,c}$ and $J^{1}_{y,c}$ for node 1, $J^{2}_{x,c}$ and $J^{2}_{y,c}$ for node 2, etc. The currents along a certain direction must have the same value (i.e., $J^{1}_{x,c} = J^{2}_{x,c}$, $J^{3}_{x,c} = J^{4}_{x,c}$, $J^{1}_{y,c} = J^{3}_{y,c}$, and $J^{2}_{y,c} = J^{4}_{y,c}$) to ensure a zero-net-leakage balance in an infinitesimally small volume containing the corner point. However, since no condition on the corner current continuity is imposed in the nodal calculation, they may be different. Using Eq. (27), four new estimates of the heterogeneous corner flux are obtained (one for each node). Taking the average of them yields

$$\Phi^{*}_{G,c} = \Phi_{G,c} + \frac{1}{4}\left[\left(J^{1}_{x,c} - J^{2}_{x,c}\right) + \left(J^{3}_{x,c} - J^{4}_{x,c}\right) + \left(J^{1}_{y,c} - J^{3}_{y,c}\right) + \left(J^{2}_{y,c} - J^{4}_{y,c}\right)\right]. \tag{28}$$

This iterative scheme converges as the sum of the differences in the net currents (i.e., the term within brackets on the right-hand side of Eq. (28)) vanishes. Assuming that Eq. (2) is the exact solution of the neutron balance equation in the nodes sharing the corner, an estimate of the net currents at the corner itself is obtained from Eq. (7). For instance, the following expression is derived for $J^{1}_{x,c}$ in node 1 (we use the nodal coordinate system of Fig. 1):

$$J^{1}_{x,c} = J^{1}_{\text{env},G,x}\left(\frac{1}{2}, -\frac{1}{2}\right) = -\frac{D^{1}_{G}}{\Delta x}\left(\sum_{i_x=1}^{N_x}\alpha^{1}_{G,x,i_x}\frac{dP_{G,i_x}}{du_x}(u_x)|_{u_x=1/2} + \sum_{\substack{c_x=1 \\ c_x+c_y\leqslant N_c}}^{N_x}\sum_{c_y=1}^{N_y}\alpha^{1}_{G,xy,c_x,c_y}\frac{dP_{G,c_x}}{du_x}(u_x)|_{u_x=1/2}P_{G,c_y}\left(-\frac{1}{2}\right)\right). \tag{29}$$

Eq. (29) ensues from the fact that the infinite-medium net current in a corner point is zero.

With the CPB approach, a new estimate $\Phi^{*}_{G,c}$ of the heterogeneous corner flux $\Phi^{\text{het}}_{G,c}$ is found at the end of each rehomogenization iteration (namely, after sweeping all the nodes) with the computed flux-variation modal coefficients. This new estimate is to be used as a known term on the right-hand side of Eq. (19) in the following rehomogenization update. At the first iteration, in which no estimate of the α coefficients is available, we use Eq. (20) or Eq. (21).

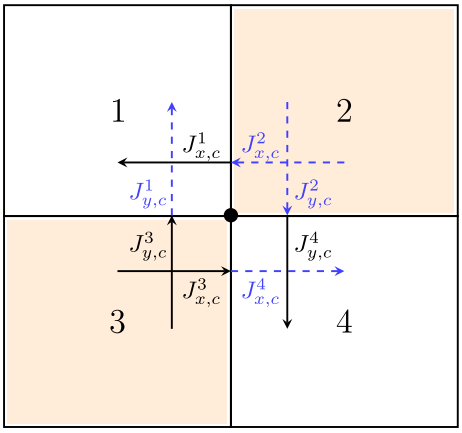

Fig. 2. Scheme of net currents in the neighborhood of a nodal corner point. The corner is shared by four nodes of two different types in a checkerboard layout.

Compared to Smith's method and the MSS, the CPB approach has a physical foundation. Moreover, it does not involve the corner discontinuity factors, so an environmental correction on these parameters is not necessary. No further approximation is introduced when solving the rehomogenization problem. On the other hand, as it will be shown in Section 3, this strategy causes a slower convergence rate of the rehomogenization algorithm due to its non-linearity. This is because the heterogeneous corner fluxes depend on the flux-variation modal coefficients, which are the unknowns of the rehomogenization linear system.

2.4. Weighted-residual balance equations

The 2-D multigroup neutron balance equation in the real environment is

$$\frac{1}{\Delta x}\frac{\partial J_{\text{env},G,x}(u_x,u_y)}{\partial u_x} + \frac{1}{\Delta y}\frac{\partial J_{\text{env},G,y}(u_x,u_y)}{\partial u_y} + \Sigma_{t,G}(u_x,u_y)\Phi_{\text{env},G}(u_x,u_y) = \sum_{G'=1}^{N_G}\left(\frac{\chi_G(u_x,u_y)}{k_{\text{eff}}}\nu\Sigma_{f,G'}(u_x,u_y) + \Sigma_{s,G'\to G}(u_x,u_y)\right)\Phi_{\text{env},G'}(u_x,u_y). \tag{30}$$

The symbols in Eq. (30) correspond to conventional notation in reactor physics literature (Stacey, 2007). Following the example of spectral rehomogenization (Gamarino et al., 2018a; Gamarino et al., 2018b), we project Eq. (30) over a set of weighting functions $W_{G,j}(u_x,u_y)$ (with j = 1,...,4) and integrate it in the two directions. The cross-section projection term for the generic reaction rate r is

$$\int_{-1/2}^{1/2}du_x\int_{-1/2}^{1/2}du_y W_{G,j}(u_x,u_y)\Sigma_{r,G}(u_x,u_y)\Phi_{\text{env},G}(u_x,u_y) = \bar{\Phi}_G h_{R,r,G,j} + \sum_{d=x,y}\sum_{i_d=1}^{N_d}\alpha_{G,d,i_d}h_{V,r,G,d,i_d,j} + \sum_{\substack{c_x=N_x \\ c_x+c_y\leqslant N_c}}^{N_x}\sum_{c_y=N_y}^{N_y}\alpha_{G,xy,c_x,c_y}h_{V,r,G,xy,c_x,c_y,j}, \tag{31}$$

where the rehomogenization coefficients are defined as

$$h_{R,r,G,j} = \int_{-1/2}^{1/2} du_x \int_{-1/2}^{1/2} du_y W_{G,j}(u_x,u_y)\Sigma_{r,G}(u_x,u_y)\varphi_{\infty,G}(u_x,u_y), \tag{32a}$$

$$h_{V,r,G,d,i_d,j} = \int_{-1/2}^{1/2} du_d P_{G,i_d}(u_d) \int_{-1/2}^{1/2} du_t W_{G,j}(u_d,u_t)\Sigma_{r,G}(u_d,u_t), \tag{32b}$$

$$h_{V,r,G,xy,c_x,c_y,j} = \int_{-1/2}^{1/2} du_x P_{G,c_x}(u_x) \int_{-1/2}^{1/2} du_y P_{G,c_y}(u_y) W_{G,j}(u_x,u_y)\Sigma_{r,G}(u_x,u_y). \tag{32c}$$

In Eq. (32b), the subscript t refers to the direction transverse to d.

The projection of the x-directional current divergence term yields (we assume again that the diffusion coefficient is spatially constant within the node)

$$\int_{-1/2}^{1/2} du_x \int_{-1/2}^{1/2} du_y W_{G,j}(u_x,u_y) \frac{\partial J_{\mathrm{env},G,x}(u_x,u_y)}{\partial u_x} = \bar{\Phi}_G h^{\infty}_{R,\mathrm{leak},G,x,j} - \frac{D_G}{\Delta x}\left[\sum_{i_x=1}^{N_x} \alpha_{G,x,i_x} h_{div,G,x,i_x,j} + \sum_{\substack{c_x=1 \\ c_x+c_y\leqslant N_c}}^{N_x}\sum_{c_y=1}^{N_y} \alpha_{G,xy,c_x,c_y} h_{div_x,G,xy,c_x,c_y,j}\right], \tag{33}$$

with the following definitions:

$$h^{\infty}_{R,\mathrm{leak},G,x,j} = \int_{-1/2}^{1/2} du_x \int_{-1/2}^{1/2} du_y W_{G,j}(u_x,u_y) \frac{\partial J_{\infty,G,x}(u_x,u_y)}{\partial u_x}, \tag{34a}$$

$$h_{div,G,x,i_x,j} = \int_{-1/2}^{1/2} du_x \frac{d^2}{du_x^2} P_{G,i_x}(u_x) \int_{-1/2}^{1/2} du_y W_{G,j}(u_x,u_y), \tag{34b}$$

$$h_{div_x,G,xy,c_x,c_y,j} = \int_{-1/2}^{1/2} du_x \frac{d^2}{du_x^2} P_{G,c_x}(u_x) \int_{-1/2}^{1/2} du_y P_{G,c_y}(u_y) W_{G,j}(u_x,u_y). \tag{34c}$$

Similar equations can be written for the divergence of the y-directional current. The rehomogenization parameter detailed in Eq. (34a) is determined for the two directions from the projection of the 2-D balance equation in the infinite medium:

$$\frac{1}{\Delta x} h^{\infty}_{R,\mathrm{leak},G,x,j} + \frac{1}{\Delta y} h^{\infty}_{R,\mathrm{leak},G,y,j} = \sum_{G'=1}^{N_G} \frac{\bar{\Phi}^{\infty}_{G'}}{\bar{\Phi}^{\infty}_{G}} \left(\frac{\chi_G}{k_\infty} h_{R,f,G',j} + h_{R,s,G'\to G,j}\right) - h_{R,t,G,j}, \tag{35}$$

where the spectral ratio $\bar{\Phi}^{\infty}_{G'}/\bar{\Phi}^{\infty}_{G}$ is computed solving the single-assembly zero-dimensional (i.e., node-averaged) neutron balance equation. In a two-group framework and with neutron emission from fission only in the fast group ($\chi_1 = 1, \chi_2 = 0$), this reads

$$\frac{\bar{\Phi}^{\infty}_1}{\bar{\Phi}^{\infty}_2} = \frac{\Sigma^{\infty}_{a,2} + \Sigma^{\infty}_{s,2\to 1} + D^{\infty}_2 B^2}{\Sigma^{\infty}_{s,1\to 2}}, \tag{36}$$

where B^2 denotes a buckling coefficient. We set $B^2 = B^2_{\mathrm{crit}}$ if the nodal cross sections are generated with the critical-spectrum correction (Hebert, 2009), or $B^2 = 0$ otherwise.

To summarize, with the above definitions the j-th weighted-residual equation is

$$\begin{aligned}
&\bar{\Phi}_G\left(\sum_{d=x,y}\frac{h^{\infty}_{R,\mathrm{leak},G,d,j}}{\Delta d} + h_{R,t,G,j}\right) + \sum_{d=x,y}\sum_{i_d=1}^{N_d}\alpha_{G,d,i_d}\left(h_{V,t,G,d,i_d,j} - \frac{D_G}{\Delta d^2}h_{div,G,d,i_d,j}\right) \\
&+ \sum_{\substack{c_x=1 \\ c_x+c_y\leqslant N_c}}^{N_x}\sum_{c_y=1}^{N_y}\alpha_{G,xy,c_x,c_y}\left(h_{V,t,G,xy,c_x,c_y,j} - D_G\sum_{d=x,y}\frac{h_{div_d,G,xy,c_x,c_y,j}}{\Delta d^2}\right) \\
&= \sum_{G'=1}^{N_G}\left[\bar{\Phi}_{G'}\left(\frac{\chi_G}{k_{\mathrm{eff}}}h_{R,f,G',j} + h_{R,s,G'\to G,j}\right)\right. \\
&+ \sum_{d=x,y}\sum_{i_d=1}^{N_d}\alpha_{G',d,i_d}\left(\frac{\chi_G}{k_{\mathrm{eff}}}h_{V,f,G',d,i_d,j} + h_{V,s,G'\to G,d,i_d,j}\right) \\
&\left.+ \sum_{\substack{c_x=1 \\ c_x+c_y\leqslant N_c}}^{N_x}\sum_{c_y=1}^{N_y}\alpha_{G',xy,c_x,c_y}\left(\frac{\chi_G}{k_{\mathrm{eff}}}h_{V,f,G',xy,c_x,c_y,j} + h_{V,s,G'\to G,xy,c_x,c_y,j}\right)\right].
\end{aligned} \tag{37}$$

Using Eq. (37), we make the assumption that the nodal estimates $\bar{\Phi}_G$ and k_{eff} satisfy the neutron balance in space [Eq. (30)] in a weighted-integral sense.

The choice of the weighting functions $W_{G,j}(u_x,u_y)$ is, in principle, arbitrary. However, these modes must be selected carefully to avoid ill-conditioning of the rehomogenization linear system that ensues from the set of equations defined above [Eqs. (13), (17), (19), and (37)]. Using Galerkin projection, the lowest condition number of the solving matrix has been achieved with the following set of test functions in one variable:

$$\begin{aligned}
W_1(u_x) = P_1(u_x), \quad W_2(u_y) = P_1(u_y), \quad W_3(u_x) \\
= P_2(u_x), \quad W_4(u_y) = P_2(u_y).
\end{aligned} \tag{38}$$

With this choice, the weighting operators do not depend on the energy group.

2.5. Summary of the procedure

At the end of a non-linear flux iteration, the nodes are swept to solve the spatial rehomogenization problem. The rehomogenization linear system is set up independently for each node with Eqs. (13), (17), (19) and (37). In Eq. (19), the corner flux is determined using (*i*) Eqs. (20)–(24), or (*ii*) Eqs. (28) and (29) with the flux-variation modal coefficients from the previous rehomogenization update. After solving the system, the new estimates of the environmental discontinuity factors at the node surfaces are determined with Eq. (9). The spatial cross-section correction for reaction r is computed as

$$\begin{aligned}
\delta\Sigma_{r,G} &= \frac{1}{\bar{\Phi}_G}\int_{-1/2}^{1/2} du_x \int_{-1/2}^{1/2} du_y \Sigma_{r,G}(u_x,u_y)\delta\Phi_G(u_x,u_y) \\
&= \sum_{d=x,y}\sum_{i_d=1}^{N_d}\alpha_{G,d,i_d}h_{V,r,G,d,i_d,0} + \sum_{\substack{c_x=1 \\ c_x+c_y\leqslant N_c}}^{N_x}\sum_{c_y=1}^{N_y}\alpha_{G,xy,c_x,c_y}h_{V,r,G,xy,c_x,c_y,0},
\end{aligned} \tag{39}$$

where the index $j = 0$ refers to the unitary weighting function [$W_{G,0}(u_d) = 1$]. When the CPB condition is applied, as the corner fluxes converge, the corrections $\delta f_{G,d\pm}$ and $\delta\Sigma_{r,G}$ also converge, and so do the effective multiplication factor and the nodal variables $\bar{\Phi}_G$, $\Phi^{\mathrm{hom}}_{G,d\pm}$, and $J_{G,d\pm}$ (which are the input quantities of the rehomogenization algorithm).

We exploit the information on the 2-D directional net current distributions [Eq. (7)] to compute the few-group transverse-leakage shape for the NEM (or the Analytic Nodal Method) equations. This approach replaces the approximation commonly adopted in industrial nodal codes, which is based on a three-

node quadratic fit along the direction of interest (Lawrence, 1986). This approximation lacks a theoretical justification and introduces an inconsistency in the solution of the nodal equations, because it uses information from the adjacent nodes in the direction under consideration to determine the internodal leakage in the transverse direction. For the 1-D transverse-integrated problem along the x direction, the transverse leakage is formulated as

$$L_{\mathrm{env},G,y}(u_x) = \frac{1}{\Delta y}\left[J_{\mathrm{env},G,y}(u_x,u_y)|_{u_y=\frac{1}{2}} - J_{\mathrm{env},G,y}(u_x,u_y)|_{u_y=-\frac{1}{2}}\right]. \tag{40}$$

Introducing Eqs. (4), (7) and (8) into Eq. (40), after some algebraic manipulation we obtain

$$L_{\mathrm{env},G,y}(u_x) = \bar{L}_{G,y} - \frac{D_G}{\Delta y^2}\sum_{c_x=1}^{N_x}\sum_{\substack{c_y=1\\ c_x+c_y\leqslant N_c}}^{N_y}\alpha_{G,xy,c_x,c_y}\, b_{G,c_y} P_{G,c_x}(u_x), \tag{41}$$

where $\bar{L}_{G,y}$ is the node-averaged leakage in the y direction (i.e., the transverse direction), and b_{G,c_y} is a constant term defined as

$$b_{G,c_y} = \frac{dP_{G,c_y}}{du_y}(u_y)|_{u_y=\frac{1}{2}} - \frac{dP_{G,c_y}}{du_y}(u_y)|_{u_y=-\frac{1}{2}}. \tag{42}$$

Setting $N_c = 4$ and limiting the order of the directional polynomial basis functions in the cross terms to 2, we obtain $b_{G,1} = 0$ and $b_{G,2} = 2$. Eq. (41) becomes thus

$$L_{\mathrm{env},G,y}(u_x) = \bar{L}_{G,y} - \frac{2D_G}{\Delta y^2}\sum_{c_x=1}^{2}\alpha_{G,xy,c_x,2} P_{c_x}(u_x). \tag{43}$$

The transverse leakage detailed in Eq. (43) is still a quadratic polynomial. However, its shape retains some information on the 2-D node-to-node leakage distribution (i.e., information from the transverse direction) via the cross coefficients $\alpha_{G,xy,c_x,2}$. In this way, the unphysical feature of the standard approximation discussed above is removed.

3. Numerical results

We validate the method on the same colorset (i.e., four-assembly) configurations considered in Gamarino et al. (2018b): (*i*) a UO_2 colorset with burnable-absorber (Pyrex) rods, (*ii*) a UO_2 colorset with AIC-type control rods, (*iii*) a UO_2 colorset with gadolinium-bearing fuel pins, and (*iv*) a UO_2/MOX colorset. Reflective boundary conditions are set at the assembly centerlines. Two-group nodal simulations are performed with the TU Delft in-house-developed BRISINGR nodal code (Gamarino et al., 2018b), which combines the conventional Coarse Mesh Finite Difference (CMFD) and NEM solution strategies. The infinite-medium homogenization parameters are generated with the APOLLO2-A deterministic lattice transport code (Martinolli et al., 2010). Since in this work we do not apply spectral rehomogenization, the critical-buckling correction (which is a default option in advanced nodal codes) is applied to the nodal cross sections (Hebert, 2009; Gamarino et al., 2018a). All the test cases are simulated in critical conditions (k_{eff}=1), which are determined with a critical-boron search, and at zero burn-up. Isothermal conditions (i.e., no thermal–hydraulic feedback) during nominal operation are considered. We use a spatial discretization of one node per assembly quarter. We present the results of the calculations with:

- single-assembly cross sections and discontinuity factors (calculation *a*);
- 2-D spatial rehomogenization of cross sections and discontinuity factors, using the CPB approach (calculation *b*) and the MSS/Smith's method (calculation *c*) to determine the corner fluxes;
- 1-D spatial rehomogenization of cross sections and discontinuity factors (calculation *d*).

For the sake of convenience, from now on we will refer to the hybrid MSS/Smith's method simply as MSS. In calculations *b* and *c*, the spatial rehomogenization coefficients [Eqs. (32) and (34)] are computed with the infinite-medium cell-homogenized cross sections and flux distribution.

The reference calculations are performed with APOLLO2-A. We test the accuracy of spatial rehomogenization on the main nodal parameters and on the pin-by-pin flux and fission-power distributions. In all the calculations, the 2-D heterogeneous intranodal flux is reconstructed with the dehomogenization method described in Joo et al. (2009). This approach is based on a 2-D, fourth-order Legendre-polynomial expansion of the neutron source distribution, which results in a semi-analytic solution of the 2-D, group-decoupled neutron diffusion equation. In calculations *b* and *c*, the corner fluxes computed with the 2-D rehomogenization are used as boundary conditions for the pin-flux reconstruction. The pin-power Root-Mean-Square (RMS) deviations are expressed in terms of the relative error ($RMS_{P,r}$) and of the power-weighted absolute error ($RMS_{P,wa}$), namely

$$RMS_{P,r} = \sqrt{\frac{1}{N_{fc}}\sum_{i=1}^{N_{fc}}\left(\frac{P_i^{\mathrm{calc}} - P_i^{\mathrm{ref}}}{P_i^{\mathrm{ref}}}\right)^2}\cdot 100\%, \tag{44a}$$

$$RMS_{P,wa} = \frac{\sqrt{\frac{1}{N_{fc}}\sum_{i=1}^{N_{fc}}\left(P_i^{\mathrm{calc}} - P_i^{\mathrm{ref}}\right)^2 \frac{P_i^{\mathrm{ref}}}{\bar{P}_{CS}^{\mathrm{ref}}}}}{\bar{P}_{CS}^{\mathrm{ref}}}\cdot 100\%, \tag{44b}$$

where N_{fc} is the number of fuel cells, P_i^{calc} and P_i^{ref} are the computed and reference (i.e., from APOLLO2-A) values of the fission power in the i-th cell, and $\bar{P}_{CS}^{\mathrm{ref}}$ is the reference average power in the colorset. With Eq. (44b), the errors in the hot spots (i.e., the fuel cells having the highest thermal load) have more weight in the accuracy assessment. We also use Eq. (44a) to compute the RMS deviation in the two-group flux distribution ($\mathrm{RMS}_{\Phi_G,r}$).

3.1. Example 1: UO_2 colorset with burnable-absorber (Pyrex) rods

The first colorset is made of four 17 × 17 PWR fuel assemblies of fresh UO_2. Two of these have 1.8% enrichment, whereas the other two have 3.1% enrichment and host 16 burnable-poison rods made of borosilicate glass (Pyrex). The colorset layout is depicted in Fig. 3.

The critical boron concentration is 1465 ppm. The reference values of the normalized fission power are 0.92 in the 1.8%-enriched assembly and 1.08 in the 3.1%-enriched poisoned assembly. For the sake of completeness, we report here the reference absorption and production cross sections (condensed and homogenized in the colorset environment) computed in APOLLO2-A: $\Sigma_{a,1} = 0.00873\,\mathrm{cm}^{-1}, \Sigma_{a,2} = 0.0686\,\mathrm{cm}^{-1}, \nu\Sigma_{f,1} = 0.00483\,\mathrm{cm}^{-1}$, and $\nu\Sigma_{f,2} = 0.0811\ \mathrm{cm}^{-1}$ in the 1.8%-enriched assembly; $\Sigma_{a,1} = 0.0101\ \mathrm{cm}^{-1}$, $\Sigma_{a,2} = 0.104\ \mathrm{cm}^{-1}, \nu\Sigma_{f,1} = 0.00657\ \mathrm{cm}^{-1}$, and $\nu\Sigma_{f,2} = 0.131\ \mathrm{cm}^{-1}$ in the 3.1%-enriched assembly with Pyrex.

Fig. 4 depicts the reference variation in the 2-D flux distribution between the real environment and the infinite lattice in the two fuel assemblies. The percent values are computed with respect to the node-averaged flux. Fig. 5 shows the flux variation computed with the 2-D spatial rehomogenization, combined with the CPB approach for the corner-point fluxes. The result of the MSS approach is not presented because the differences are small. Rehomogenization captures the overall flux variation reasonably well. The main differences between the reference and computed

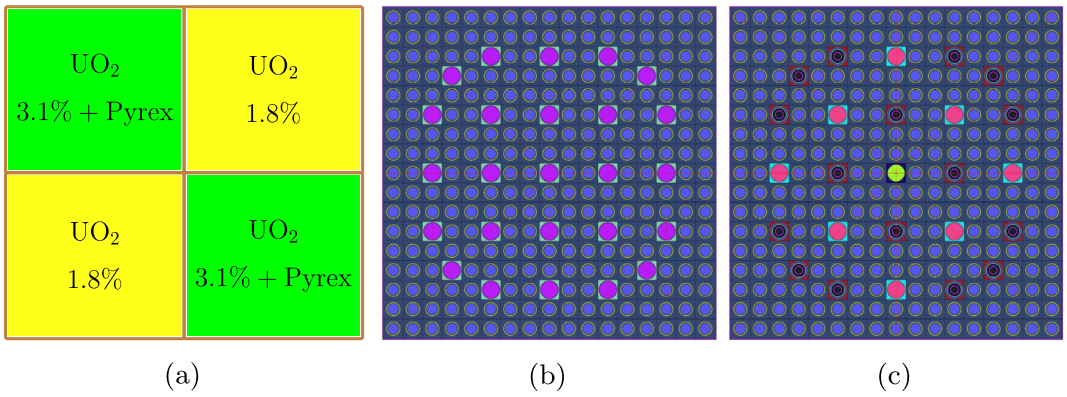

Fig. 3. (a) Assembly set of Example 1. Layout of the UO_2 fuel assemblies: (b) with 1.8% enrichment, (c) with 3.1% enrichment and 16 burnable-poison rods. The two bundles host 24 and 8 empty guide tubes, respectively, which are made of the Zircaloy-4 alloy. An empty instrumentation tube is present at the center of both assemblies.

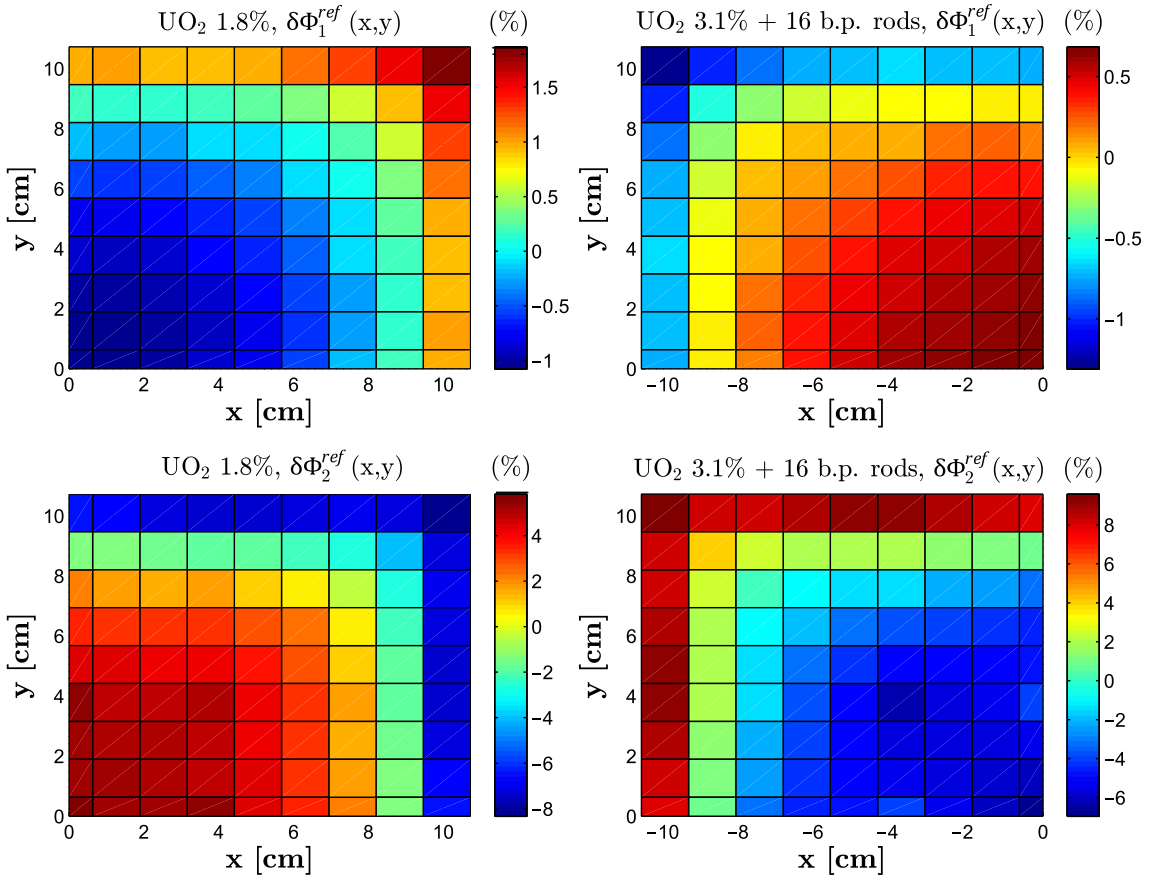

Fig. 4. Example 1: reference variation (in percentage) in the 2-D pin-by-pin flux between the environmental and infinite-lattice conditions in the neighboring quarters of the two dissimilar assemblies. The top and bottom plots depict the variations in the fast and thermal groups, respectively. The plots on the left side refer to the 1.8%-enriched assembly quarter, whereas those on the right side refer to the 3.1%-enriched assembly quarter. The coordinates [0,0] (in cm) correspond to the assembly centers. The abscissas 10.1 cm in the 1.8%-enriched assembly and −10.1 cm in the assembly with Pyrex denote the centers of the corresponding outer pin rows (the water gap is not shown).

distributions are observed in the outer pin rows of both assemblies. In the 1.8%-enriched bundle, the magnitude of the thermal flux change is overestimated at the assembly edges and underestimated in the external-corner fuel cell. The opposite is found in the assembly with Pyrex rods. Fig. 6 shows the variation in the transverse-integrated flux $\Phi_{G,x}(x)$ computed with the 1-D reho-mogenization. For the sake of comparison, we also plot the 1-D curves obtained by transverse integration of the 2-D distributions of Fig. 5. The deviations between the 1-D and 2-D approaches are not significant. They are more evident in the fast group, especially in the assembly with Pyrex.

Table 1 reports the number of non-linear flux iterations (N_{iter}) and the errors in the integral parameters and main nodal cross sections (the errors in the discontinuity factors will be addressed in Section 4.2). Compared to the calculation with infinite-medium cross sections and discontinuity factors, both the 2-D and 1-D models give a significantly more accurate prediction of the multiplication factor and fission power. Much of this

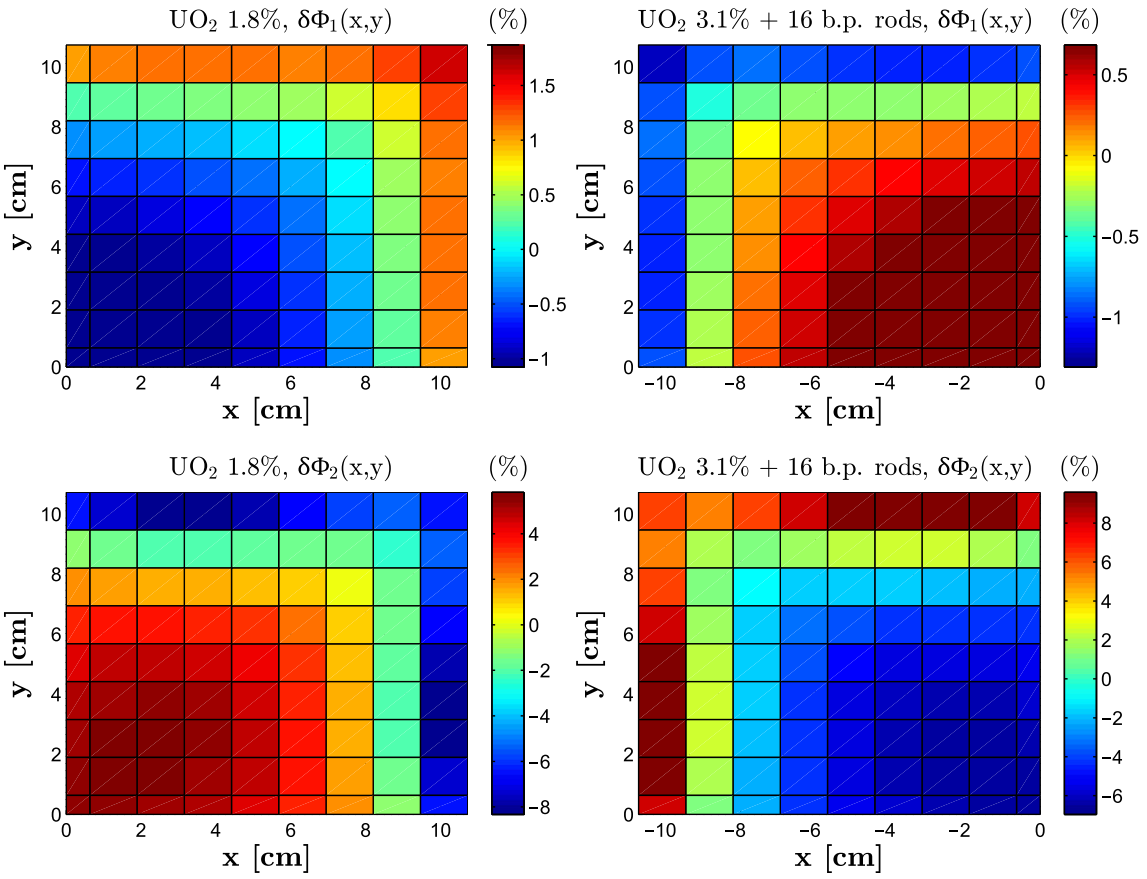

Fig. 5. Example 1: variation (in percentage) in the 2-D flux distribution in the neighboring quarters of the two assemblies, as computed with the CPB-based 2-D rehomogenization. The results are plotted with the same scale as in Fig. 4 to ease the comparison between the reference and computed variations.

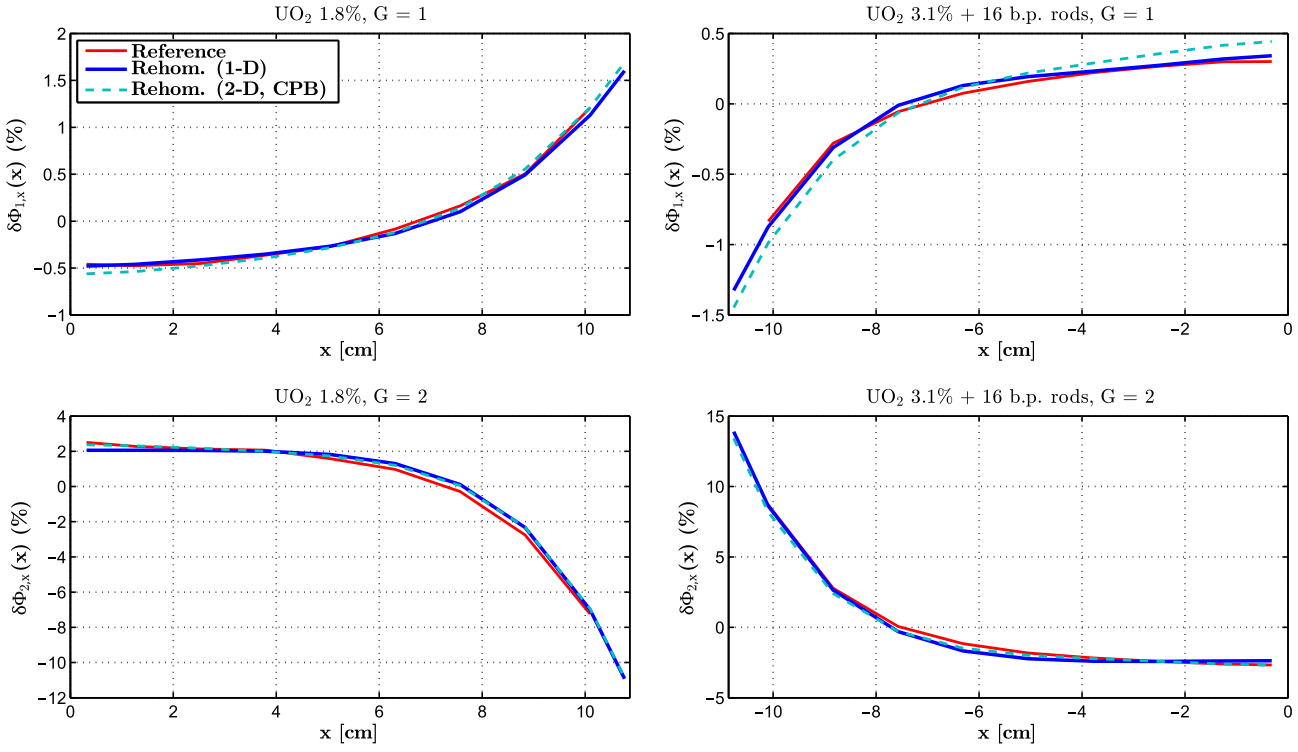

Fig. 6. Example 1: variation (in percentage) in the transverse-integrated flux distribution in the neighboring quarters of the two assemblies. The computed variation in the water gap is also depicted.

Table 1
Example 1: (a) number of non-linear flux iterations and errors in the integral parameters, and (b) errors in the absorption and production nodal cross sections. The values of the power error within parentheses refer to the fast- and thermal-group power.

(a)

Simulation	N_{iter}	Δk_{eff} [pcm]	UO_2 1.8% $\Delta\overline{P}_{fiss}$ (%)	UO_2 3.1% + 16 b.p. rods $\Delta\overline{P}_{fiss}$ (%)
No rehom. (*a*)	9	−189	0.85 (0.86, 0.85)	−0.72 (−0.60, −0.76)
2-D rehom. – CPB (*b*)	15	26	0.19 (0.74, 0.06)	−0.16 (−0.52, −0.05)
2-D rehom. – MSS (*c*)	12	30	0.22 (0.78, 0.08)	−0.18 (−0.55, −0.07)
1-D rehom. (*d*)	13	−18	0.39 (0.87, 0.28)	−0.33 (−0.61, −0.25)

(b)

	UO_2 1.8%				UO_2 3.1% + 16 b.p. rods			
	Errors (%)							
Simulation	$\Delta\Sigma_{a,1}$	$\Delta\Sigma_{a,2}$	$\Delta\nu\Sigma_{f,1}$	$\Delta\nu\Sigma_{f,2}$	$\Delta\Sigma_{a,1}$	$\Delta\Sigma_{a,2}$	$\Delta\nu\Sigma_{f,1}$	$\Delta\nu\Sigma_{f,2}$
No rehom. (*a*)	−0.04	0.69	0.51	0.81	0.10	−0.50	−0.33	−1.03
2-D rehom. – CPB (*b*)	−0.02	0.64	0.53	0.71	0.11	−0.92	−0.34	−0.90
2-D rehom. – MSS (*c*)	−0.02	0.64	0.53	0.71	0.11	−0.93	−0.34	−0.90
1-D rehom. (*d*)	−0.03	0.64	0.53	0.70	0.11	−0.85	−0.34	−0.93

Table 2
Example 1: errors in the absorption and production cross sections rehomogenized with the reference 2-D flux variation and with a least-squares best fit of it.

	UO_2 1.8%				UO_2 3.1% + 16 b.p. rods			
	Errors (%)							
Flux variation (2-D)	$\Delta\Sigma_{a,1}$	$\Delta\Sigma_{a,2}$	$\Delta\nu\Sigma_{f,1}$	$\Delta\nu\Sigma_{f,2}$	$\Delta\Sigma_{a,1}$	$\Delta\Sigma_{a,2}$	$\Delta\nu\Sigma_{f,1}$	$\Delta\nu\Sigma_{f,2}$
Reference	−0.01	0.53	0.55	0.50	0.09	−0.68	−0.35	−0.71
Best fit	−0.02	0.62	0.53	0.67	0.11	−0.84	−0.34	−0.86

improvement comes from the correction of the thermal absorption cross section in the assembly with burnable poison, even if the corresponding error becomes higher than that of the single-assembly estimate. The increase in the error in this cross section is because of the exclusion of spectral effects, which go in the opposite direction to spatial ones (see Section 4.4). The improvement in the power is more apparent with the 2-D rehomogenization. The differences between the CPB and MSS strategies are negligible.

Table 2 compares the errors in the cross sections rehomogenized with (*i*) the reference 2-D flux change (Fig. 4) and (*ii*) a least-squares best fit of it. The best fit has been computed with the basis functions defined in Eq. (5), using the same number of directional and cross terms as in the modal reconstruction [Eq. (4)]. Since these two sets of cross sections do not account for the spectral effects of the environment, they can be considered as a reference to assess the accuracy of spatial rehomogenization. Comparing Tables 1 and 2, it turns out that the cross-section corrections computed with the 2-D rehomogenization go in the right direction and are very close to those obtained with a best fit of the 2-D reference. The inaccuracy in the flux-change reconstruction observed in Fig. 5 is therefore ascribable to the limited fitting capability of the 1-D basis functions [Eq. (5)] rather than to a deficiency of the method. We have verified that increasing the number of cross terms in the best fit from four to six or eight improves the computed corrections only slightly. Rehomogenization underestimates the corrections on $\Sigma_{a,2}$ and $\nu\Sigma_{f,2}$ in the 1.8%-enriched assembly and on $\nu\Sigma_{f,2}$ in the assembly with Pyrex (see Tables 1(b) and 2). It overcorrects $\Sigma_{a,2}$ in the latter. This overcorrection is due to an overly negative estimate of the flux variation in the center of the assembly, where the Pyrex rods are located and thermal absorption is higher. This mismatch is smaller with the 1-D model. The flux spatial variation has no effect on the fast-group cross sections. The same has been observed in fast-to-thermal scattering and in the diffusion coefficients of both energy groups, which are not reported in the previous tables. For these quantities, both the reference and computed corrections are negligible.

Fig. 7 compares the relative errors in the thermal-flux pin-by-pin distribution of the 1.8%-enriched assembly, as computed with calculations *a* and *b*. A general improvement is observed, especially in the fuel cells surrounding the assembly external vertex. The reference fission-power distribution and the corresponding relative errors are in Figs. 8 and 9, respectively. Table 3 shows the RMS errors in the two-group flux and total power. The reduction in the RMS deviations is apparent in the poison-free bundle, whereas it is less evident in the assembly with Pyrex. The error in the fuel cell with the highest power (i.e., the external-corner cell in the assembly with Pyrex) increases from −0.64% to −1.71% when the 2-D rehomogenization is applied (Fig. 9).

3.2. Example 2: UO_2 colorset with AIC-type control rods

In this test case, two banks of twenty-four black control rods each are inserted into two of the four fuel assemblies. The type of the control elements is AIC (silver-indium-cadmium), with the following mass percent composition: 80% ^{47}Ag, 15% ^{48}Cd, and 5% ^{49}In. The ^{235}U enrichment is 1.8% in the unrodded assembly and 2.4% in the rodded one. The colorset layout is shown in Fig. 10. The critical configuration is achieved with a boron concentration of 222 ppm. The reference values of the normalized fission power are 1.12 in the unrodded assembly and 0.88 in the rodded one. The reference cross sections are: $\Sigma_{a,1} = 0.00833\ \text{cm}^{-1}$, $\Sigma_{a,2} = 0.0573\ \text{cm}^{-1}$, $\nu\Sigma_{f,1} = 0.00483\ \text{cm}^{-1}$, and $\nu\Sigma_{f,2} = 0.0828\ \text{cm}^{-1}$ in the unrodded assembly; $\Sigma_{a,1} = 0.0119\ \text{cm}^{-1}$, $\Sigma_{a,2} = 0.0942\ \text{cm}^{-1}$, $\nu\Sigma_{f,1} = 0.00554\ \text{cm}^{-1}$, and $\nu\Sigma_{f,2} = 0.109\ \text{cm}^{-1}$ in the rodded assembly.

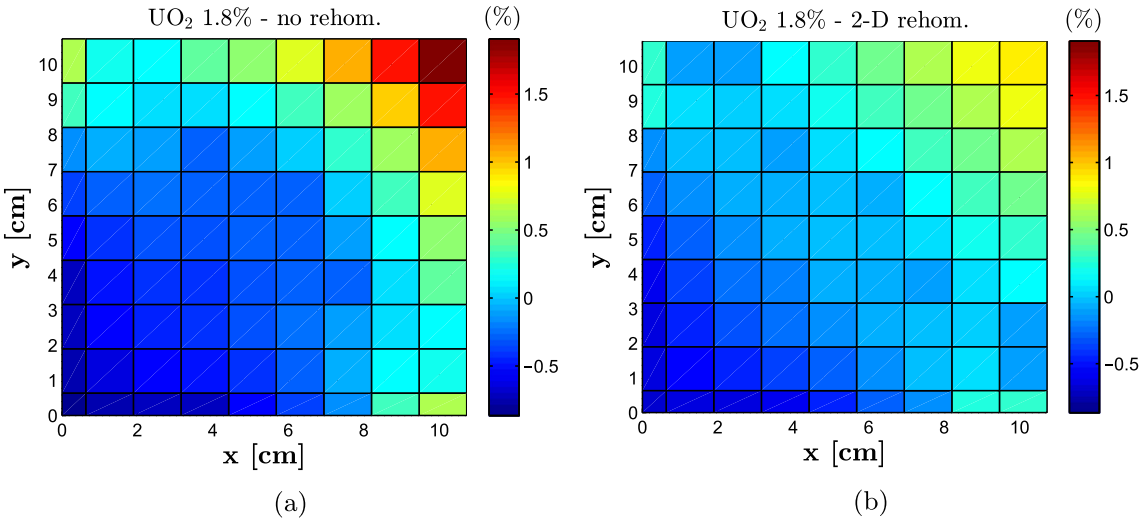

Fig. 7. Example 1: relative error (in percentage) in the pin-by-pin thermal flux in the 1.8%-enriched assembly quarter. The plots refer to the calculations (a) without rehomogenization and (b) with the CPB-based 2-D rehomogenization.

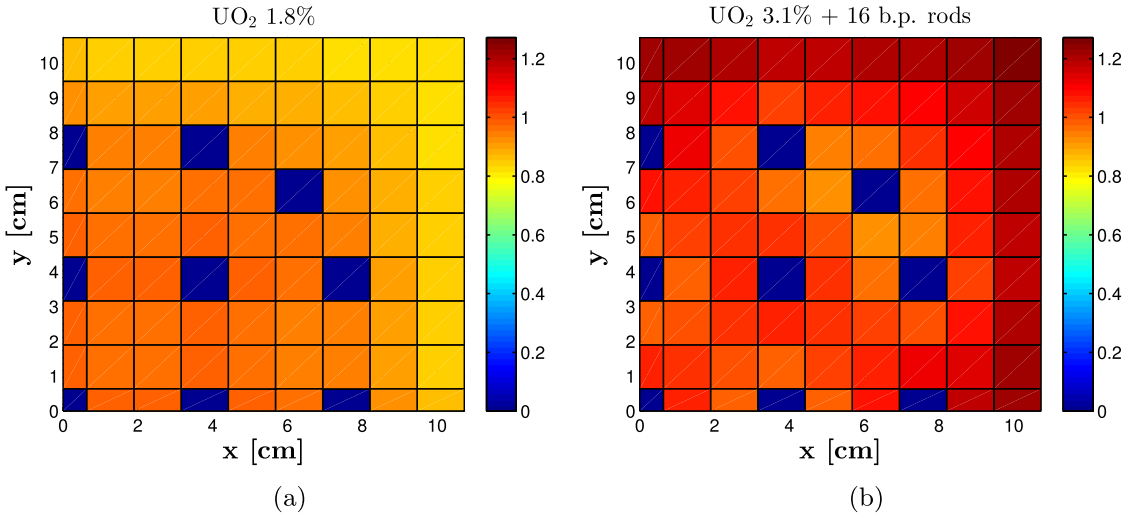

Fig. 8. Example 1: reference pin power (normalized to the colorset-averaged value) in (a) the 1.8%-enriched assembly and (b) the 3.1%-enriched assembly with Pyrex rods.

The reference and computed 2-D flux variations are in Figs. 11 and 12. The prediction is quite accurate in the unrodded assembly. In the rodded bundle, the magnitude of the flux change is underestimated around the external corner, where it is positive, and overestimated in the control-rod cells closer to the assembly center (i.e., at the coordinates [−3.79, 0], [−3.79, 3.79] and [0, 3.79] cm), where it is negative. The decrease in thermal absorption in the environment is therefore overestimated (see Tables 4 and 5). The variation in the transverse-integrated flux is shown in Fig. 13. In the thermal group of the rodded assembly, the 1-D curve from the 2-D model approximates the reference better in the neighborhood of the coordinate −3.79 cm, which spans three rodded cells along the y direction (see Figs. 10(c) and 11). However, it provides a less accurate estimate at the periphery.

Tables 4 and 5 report the errors in the nodal quantities. Also in this case, an improvement in k_{eff} and in the fission power is observed, particularly with the 1-D rehomogenization. Calculations b, c and d mainly differ in the prediction of the correction $\delta\Sigma_{a,2}$ in the rodded assembly, which is overestimated to a different extent in the three cases (see Tables 4(b) and 5). As in the example with Pyrex rods, the 2-D model reproduces faithfully the corrections computed with a best fit of the reference flux change. Therefore, the overestimation of $\delta\Sigma_{a,2}$ is mostly because the basis functions cannot reconstruct the dip in $\delta\Phi_2(x,y)$ in the inner rodded cells.

The relative errors in the pin-by-pin thermal flux in the unrodded assembly and in the power distribution are depicted in Figs. 14 and 16. The reference fission power is in Fig. 15. Table 6 summarizes the RMS deviations. With the 2-D model, a general improvement is only found in the unrodded bundle, even though not in the cells with higher power. Since in this assembly the 2-D rehomogenization provides a better intranodal flux distribution than calculation a (see Fig. 14), the observed increase in $\text{RMS}_{P,wa}$ is probably due in part to the inaccuracy in the infinite-medium pin-by-pin fission cross sections. With the 1-D approach, the improvement is negligible in both assemblies. The highest power (126% of the colorset-averaged value) is found in the external-corner cell of the rodded assembly and in the two cells adjacent to the empty instrumentation tube at the center of the unrodded bundle (i.e., at [0,0] cm). With the 2-D rehomogenization, the power error

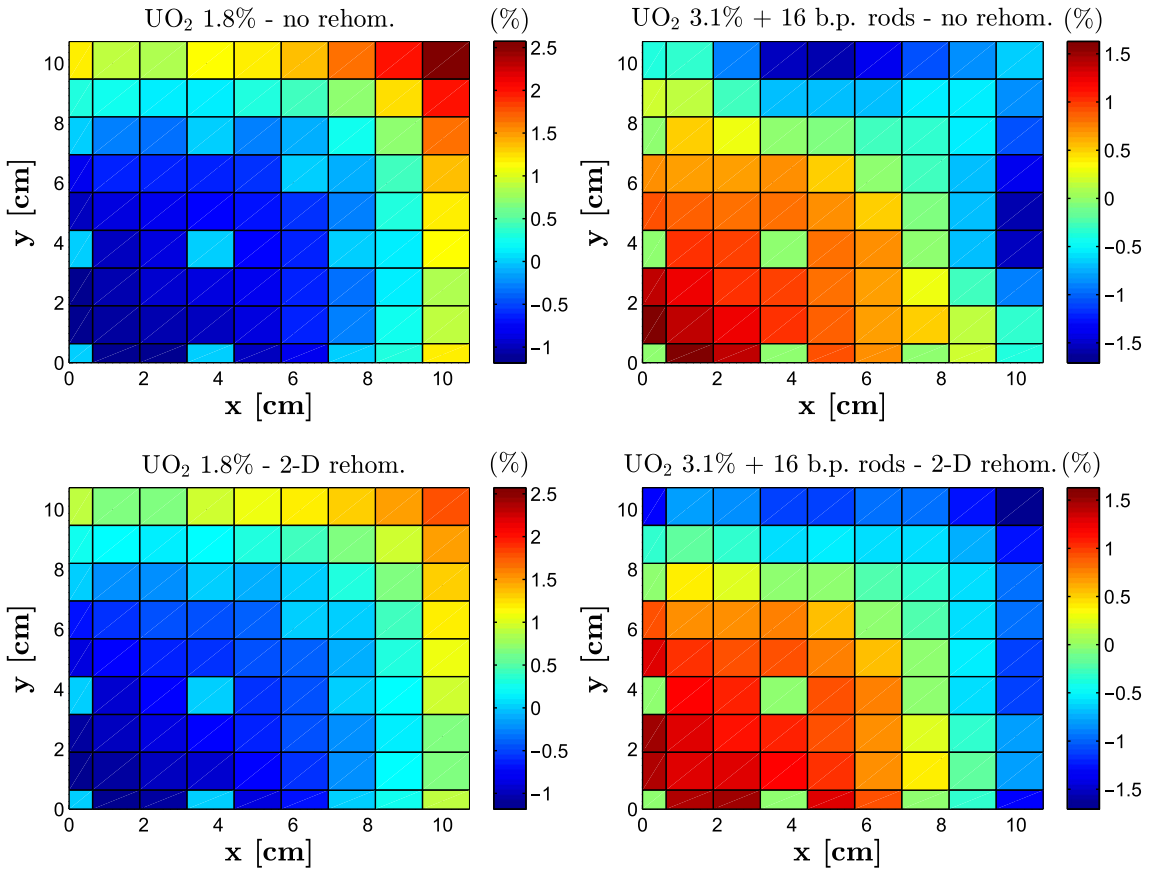

Fig. 9. Example 1: relative error (in percentage) in the pin-power distribution computed with calculations *a* and *b*.

Table 3
Example 1: RMS deviations (in percentage) in the pin-by-pin two-group flux and total fission power.

	UO_2 1.8%				UO_2 3.1% + 16 b.p. rods			
Simulation	$RMS_{\Phi_1,r}$	$RMS_{\Phi_2,r}$	$RMS_{P,r}$	$RMS_{P,wa}$	$RMS_{\Phi_1,r}$	$RMS_{\Phi_2,r}$	$RMS_{P,r}$	$RMS_{P,wa}$
No rehom. (*a*)	0.11	0.58	0.94	0.94	0.20	0.45	0.77	1.25
2-D rehom. – CPB (*b*)	0.14	0.36	0.77	0.66	0.27	0.43	0.91	1.06
1-D rehom. (*d*)	0.08	0.51	0.85	0.73	0.22	0.34	0.81	0.98

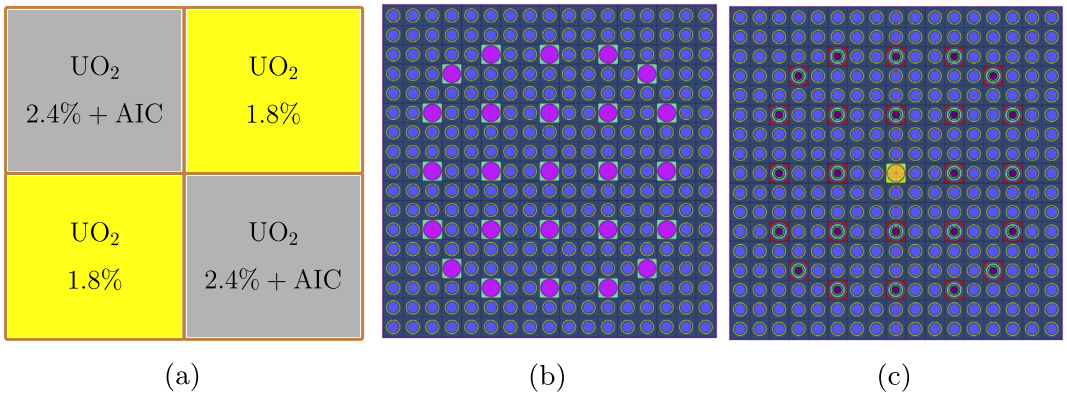

Fig. 10. (a) Assembly set of Example 2. Layout of the UO_2 fuel assemblies: (b) unrodded, and (c) rodded. The former hosts 24 empty guide tubes, whereas in the latter only the central instrumentation tube is free of control elements.

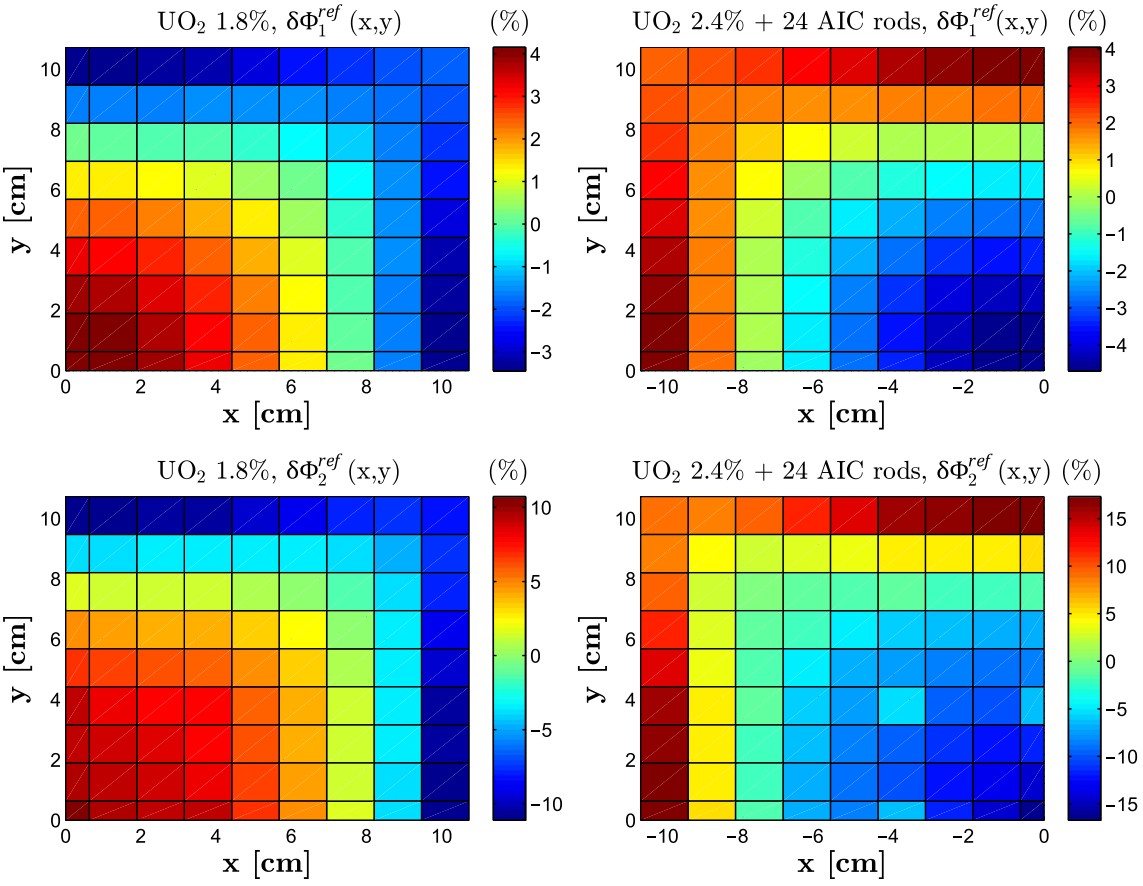

Fig. 11. Example 2: reference variation (in percentage) in the 2-D flux distribution.

decreases (in absolute value) from 3.38% to −1.0% in the former and increases (in absolute value) from −0.70% to −0.76% in the latter.

3.3. Example 3: UO_2 colorset with gadolinium-bearing fuel pins

This example (Fig. 17) is made of two 17 × 17 UO_2 assemblies with 1.8% enrichment and two 17 × 17 UO_2 assemblies with 3.9% enrichment and 12 gadolinium-bearing fuel rods. The poisoned pins have 0.25% ^{235}U enrichment and 8% mass content of gadolinium oxide (Gd_2O_3), with the isotopic composition of naturally occurring gadolinium. They are located at the periphery of the assemblies, in the outer and first inboard pin rows. The concentration of soluble boron in the moderator is 1830 ppm. The reference normalized fission power and cross sections are: $\overline{P}_{\text{fiss}} = 0.81$, $\Sigma_{a,1} = 0.00889\ \text{cm}^{-1}$, $\Sigma_{a,2} = 0.0723\ \text{cm}^{-1}$, $\nu\Sigma_{f,1} = 0.00483\ \text{cm}^{-1}$, and $\nu\Sigma_{f,2} = 0.0803\ \text{cm}^{-1}$ in the 1.8%-enriched assembly; $\overline{P}_{\text{fiss}} = 1.19$, $\Sigma_{a,1} = 0.0103\ \text{cm}^{-1}$, $\Sigma_{a,2} = 0.118\ \text{cm}^{-1}$, $\nu\Sigma_{f,1} = 0.00738\ \text{cm}^{-1}$, and $\nu\Sigma_{f,2} = 0.151\ \text{cm}^{-1}$ in the assembly with gadolinium-bearing fuel pins.

The reference and computed flux changes are shown in Figs. 18–20. The nodal errors are in Tables 7 and 8. With the 2-D model, the computed $\delta\Sigma_{a,2}$ in the 3.9%-enriched assembly is higher than the expected value. This is because the thermal-flux variation is overestimated in the gadolinium-bearing fuel pins located in the outer rows (at the coordinates [−2.53, 10.78] and [−10.78, 2.53] cm). In these cells the reference flux change is 8.12%, whereas the computed one is 13.4%. In the same fuel bundle, the correction on $\nu\Sigma_{f,2}$ goes in the wrong direction because of the combined underestimation and overestimation of the magnitude of $\delta\Phi_2(x,y)$ in the neighborhood of the assembly vertex and in the assembly center, respectively. Despite the above mismatches, the 2-D model significantly improves the k_{eff} and nodal-power estimates compared to the calculation without rehomogenization. These parameters improve less with the 1-D model. Figs. 21 and 22 show the reference fission-power distribution and the corresponding relative errors. Table 9 summarizes the RMS deviations. Rehomogenization better predicts the fission power in the center of the gadolinium-bearing assembly quarter (where the power is higher), which results in a reduction in $\text{RMS}_{P,wa}$.

3.4. Example 4: UO_2/MOX colorset

This colorset is made of two 18 × 18 UO_2 assemblies and two 18 × 18 MOX assemblies. The ^{235}U enrichment in the UO_2 assemblies is 2.1%. The MOX bundle contains three different types of fuel pins: with low plutonium content (1.78% ^{239}Pu, 0.22% ^{235}U) at the assembly corners, with intermediate plutonium content (2.53% ^{239}Pu, 0.21% ^{235}U) along the assembly outer edges, and with high plutonium content (3.86% ^{239}Pu, 0.20% ^{235}U) in the remainder of the fuel bundle. The colorset and assembly layouts are shown in Fig. 23. The concentration of diluted boron in the moderator is 2907 ppm. The reference normalized fission power and cross sections are: $\overline{P}_{\text{fiss}} = 0.85$, $\Sigma_{a,1} = 0.00924\ \text{cm}^{-1}$, $\Sigma_{a,2} = 0.0887\ \text{cm}^{-1}$, $\nu\Sigma_{f,1} = 0.00543\ \text{cm}^{-1}$, and $\nu\Sigma_{f,2} = 0.0974\ \text{cm}^{-1}$ in the UO_2 assembly; $\overline{P}_{\text{fiss}} = 1.15$, $\Sigma_{a,1} = 0.0143\ \text{cm}^{-1}$, $\Sigma_{a,2} = 0.258\ \text{cm}^{-1}$, $\nu\Sigma_{f,1} = 0.00994\ \text{cm}^{-1}$, and $\nu\Sigma_{f,2} = 0.372\ \text{cm}^{-1}$ in the MOX assembly.

Figs. 24–26 compare the results of rehomogenization with the reference flux spatial deformations. Tables 10 and 11 show the

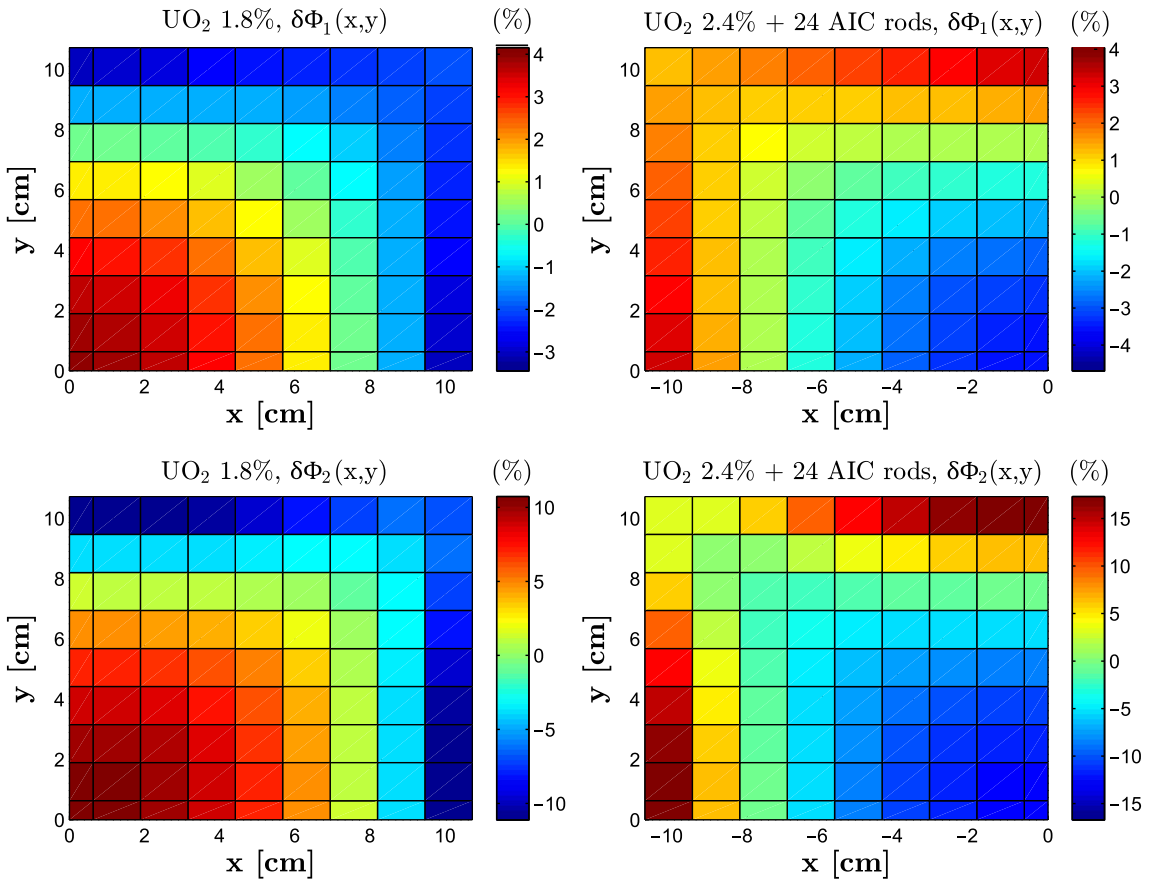

Fig. 12. Example 2: variation (in percentage) in the 2-D flux distribution, as computed with the CPB-based 2-D rehomogenization.

Table 4
Example 2: (a) number of non-linear flux iterations and errors in the integral parameters, and (b) errors in the absorption and production nodal cross sections.

(a)

Simulation	N_{iter}	Δk_{eff} [pcm]	UO_2 1.8% $\Delta\overline{P}_{fiss}$ (%)	UO_2 2.4% + 24 AIC rods $\Delta\overline{P}_{fiss}$ (%)
No rehom. (*a*)	10	−608	1.41 (0.69, 1.57)	−1.79 (−0.66, −2.15)
2-D rehom. – CPB (*b*)	18	−18	−0.72 (−0.41, −0.78)	0.92 (0.40, 1.07)
2-D rehom. – MSS (*c*)	16	−21	−0.96 (−0.64, −1.02)	1.23 (0.61, 1.40)
1-D rehom. (*d*)	16	−72	0.10 (0.21, 0.08)	−0.12 (−0.20, −0.11)

(b)

	UO_2 1.8%				UO_2 2.4% + 24 AIC rods			
	Errors (%)							
Simulation	$\Delta\Sigma_{a,1}$	$\Delta\Sigma_{a,2}$	$\Delta\nu\Sigma_{f,1}$	$\Delta\nu\Sigma_{f,2}$	$\Delta\Sigma_{a,1}$	$\Delta\Sigma_{a,2}$	$\Delta\nu\Sigma_{f,1}$	$\Delta\nu\Sigma_{f,2}$
No rehom. (*a*)	−0.72	0.66	0.11	0.72	1.31	0.63	0.10	−1.21
2-D rehom. - CPB (*b*)	−0.75	0.54	0.06	0.58	1.09	−1.42	0.16	−0.98
2-D rehom. - MSS (*c*)	−0.75	0.55	0.07	0.59	1.08	−1.51	0.16	−0.98
1-D rehom. (*d*)	−0.75	0.53	0.06	0.56	1.02	−1.02	0.18	−1.08

Table 5
Example 2: errors in the absorption and production cross sections rehomogenized with the reference 2-D flux variation and with a least-squares best fit of it.

	UO_2 1.8%				UO_2 2.4% + 24 AIC rods			
	Errors (%)							
Flux variation (2-D)	$\Delta\Sigma_{a,1}$	$\Delta\Sigma_{a,2}$	$\Delta\nu\Sigma_{f,1}$	$\Delta\nu\Sigma_{f,2}$	$\Delta\Sigma_{a,1}$	$\Delta\Sigma_{a,2}$	$\Delta\nu\Sigma_{f,1}$	$\Delta\nu\Sigma_{f,2}$
Reference	−0.80	0.35	0.01	0.33	1.08	−0.62	0.23	−0.81
Best fit	−0.76	0.51	0.06	0.53	1.04	−1.45	0.19	−0.91

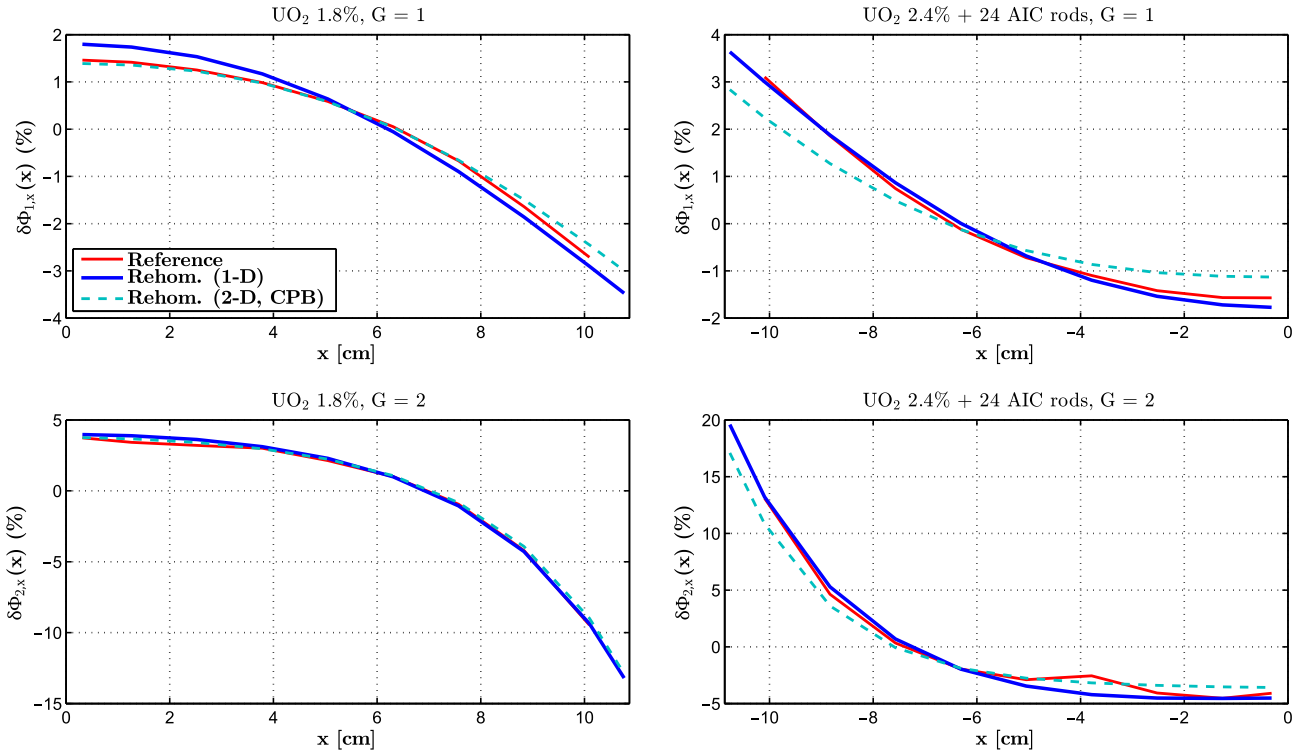

Fig. 13. Example 2: variation in the transverse-integrated flux distribution.

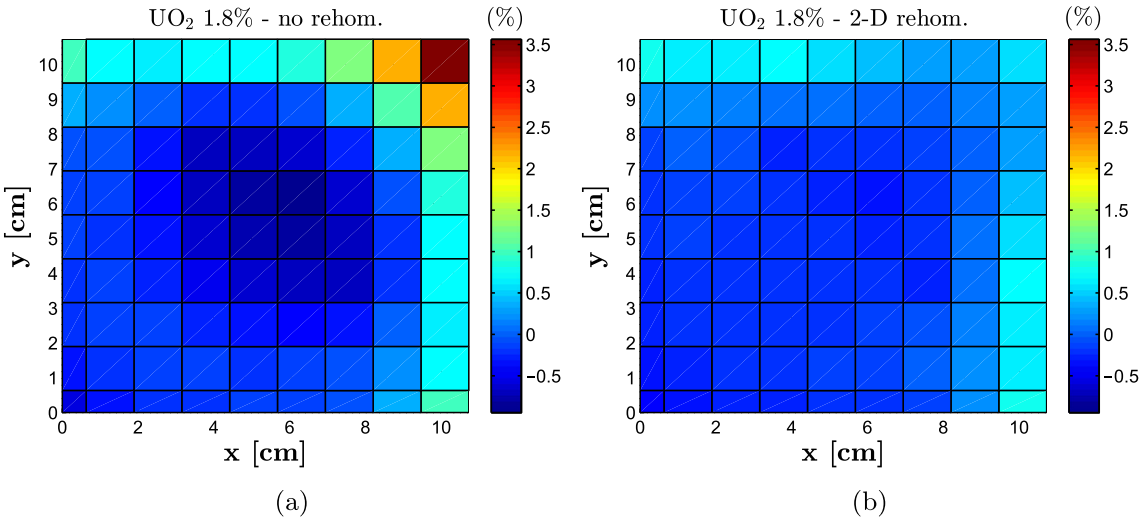

Fig. 14. Example 2: relative error (in percentage) in the pin-by-pin thermal flux in the unrodded-assembly quarter. The plots refer to the calculations (a) without rehomogenization and (b) with the CPB-based 2-D rehomogenization.

nodal errors. The 2-D model overestimates the absolute value of the flux change (which is negative) in the center of the MOX assembly. Here the plutonium content is higher (see Fig. 23(c)), and so are the thermal-group absorption and production pin-by-pin cross sections. The corrections on the thermal cross sections are thus considerably higher than those computed with the reference flux variation and, in this case, also with a least-squares best fit of it. The error in k_{eff} increases, whereas the errors in the fission power still decrease significantly.

The pin-by-pin errors are shown in Figs. 27–30 and in Table 12. In spite of the limited accuracy in the prediction of the flux variation, the flux and power distributions in the MOX assembly improve with the 2-D rehomogenization. An increase in the error is only found around the four nodal vertices, particularly in the two cells surrouding the central water-carrying instrumentation tube (in the SW corner of the quadrant). These observations are confirmed by the RMS deviations, which also decrease appreciably. The improvement is more significant in the UO_2 assembly with the 2-D model.

In this test case, the CPB-based 2-D rehomogenization has a considerably slower convergence rate than the MSS approach and the 1-D rehomogenization (Table 10).

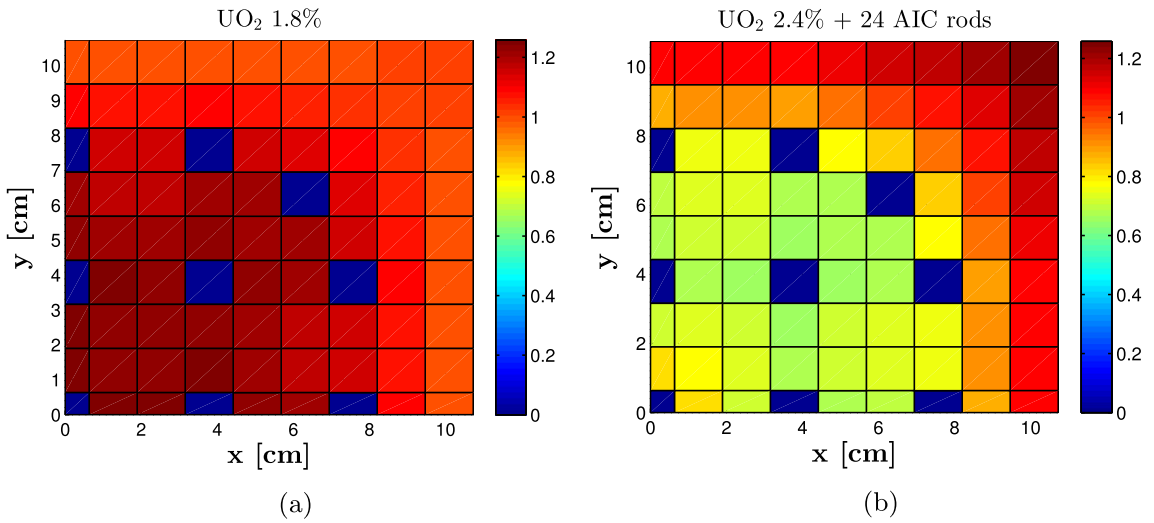

Fig. 15. Example 2: reference pin power (normalized to the colorset-averaged value) in the (a) unrodded and (b) rodded assemblies.

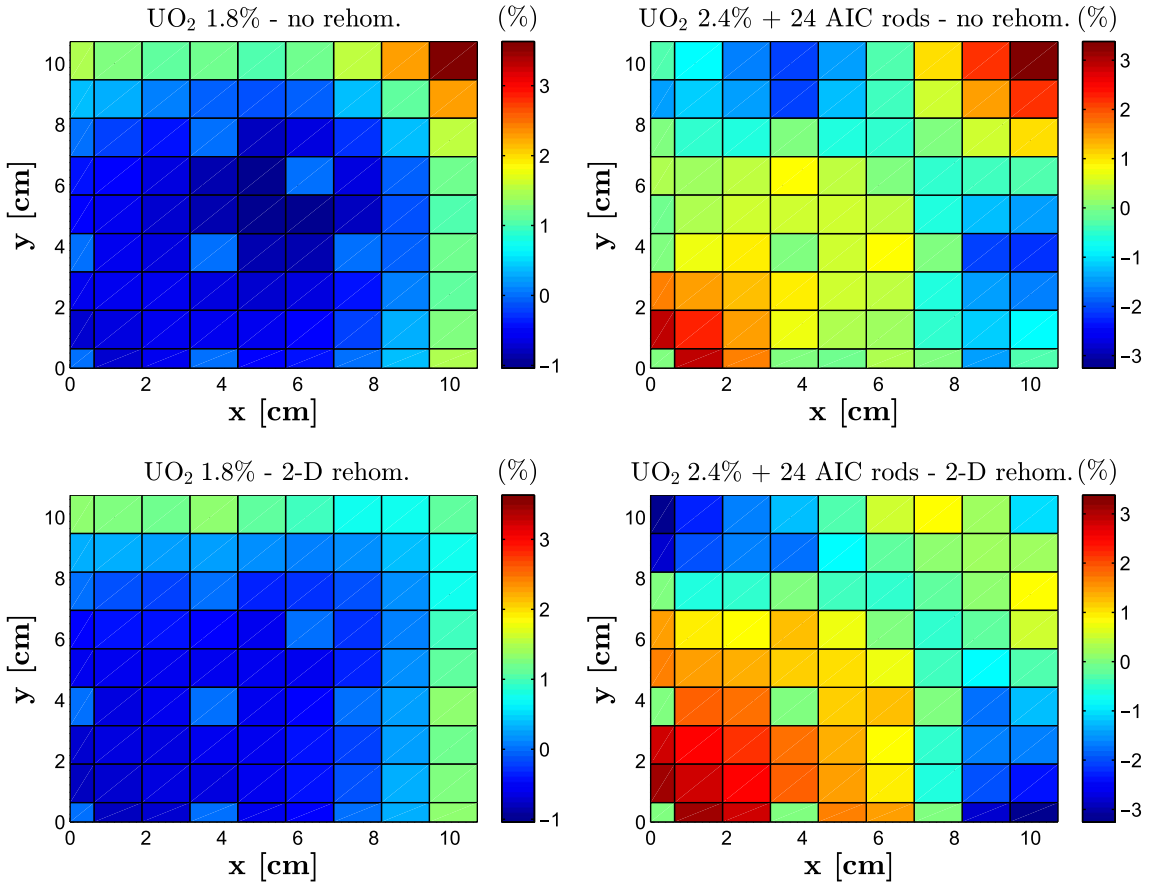

Fig. 16. Example 2: relative error (in percentage) in the pin-power distribution computed with calculations *a* and *b*.

Table 6
Example 2: RMS deviations (in percentage) in the pin-by-pin two-group flux and total fission power.

	UO_2 1.8%				UO_2 2.4% + 24 AIC rods			
Simulation	$RMS_{\Phi_1,r}$	$RMS_{\Phi_2,r}$	$RMS_{P,r}$	$RMS_{P,wa}$	$RMS_{\Phi_1,r}$	$RMS_{\Phi_2,r}$	$RMS_{P,r}$	$RMS_{P,wa}$
No rehom. (*a*)	0.20	0.78	0.96	1.28	0.43	1.31	1.25	1.50
2-D rehom. - CPB (*b*)	0.18	0.33	0.68	1.81	0.54	1.45	1.60	1.75
1-D rehom. (*d*)	0.14	0.72	0.90	1.23	0.34	1.30	1.35	1.37

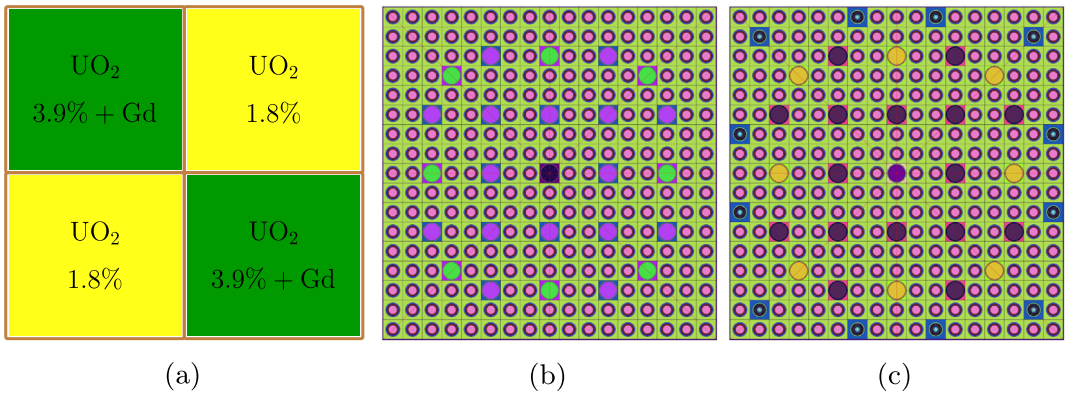

Fig. 17. (a) Assembly set of Example 3. Layout of the UO_2 fuel assemblies: (b) with 1.8% enrichment, (c) with 3.9% enrichment and 12 gadolinium-bearing fuel rods at the periphery. Both assemblies host 24 empty guide tubes and an empty instrumentation tube at the center.

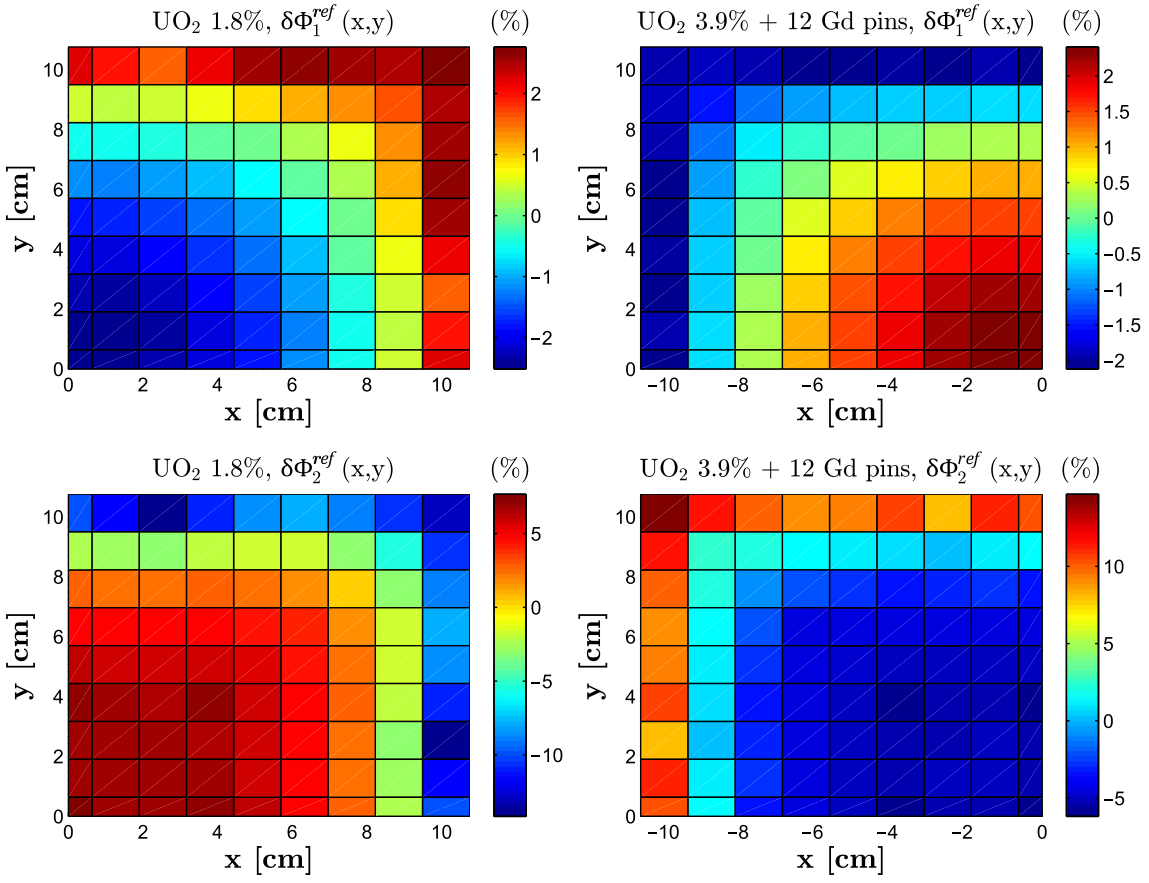

Fig. 18. Example 3: reference variation (in percentage) in the 2-D flux distribution.

4. Discussion

4.1. On the transverse-leakage approximation

As mentioned in Section 2.5, the conventional three-node quadratic fit for the approximation of the transverse-leakage distribution is a non-consistent feature of nodal calculations (Lawrence, 1986). Various methods can be found in the literature to relax this approximation (Prinsloo et al., 2014). In this section, we compare the transverse-leakage distributions computed with the aforementioned standard approach and with the quadratic approximation ensuing from the 2-D rehomogenization [Eq. (43)]. The impact of these two strategies on the nodal simulations is also addressed.

Fig. 31 shows the transverse-leakage shape $L_{G,y}(x)$ in the 1.8%-enriched UO_2 assembly of Example 1. The curves of calculations *a* and *d* have been computed with the three-node parabolic fit, whereas the curves of calculation *b* have been determined with Eq. (43). The distributions obtained with the 2-D rehomogenization differ significantly from those of the standard approximation, especially in the thermal group.

We have found that, when spatial rehomogenization is applied, the nodal calculation becomes insensitive to the transverse-

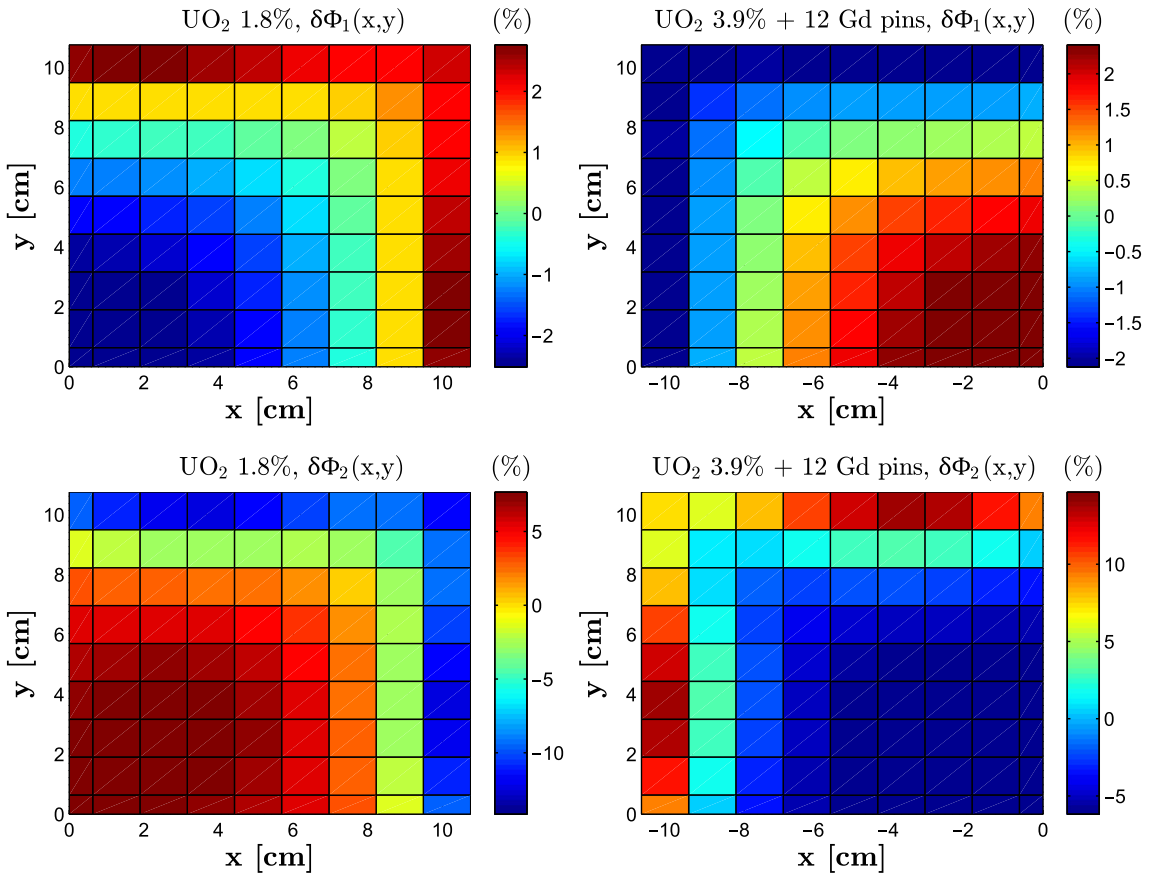

Fig. 19. Example 3: variation (in percentage) in the 2-D flux distribution, as computed with the CPB-based 2-D rehomogenization.

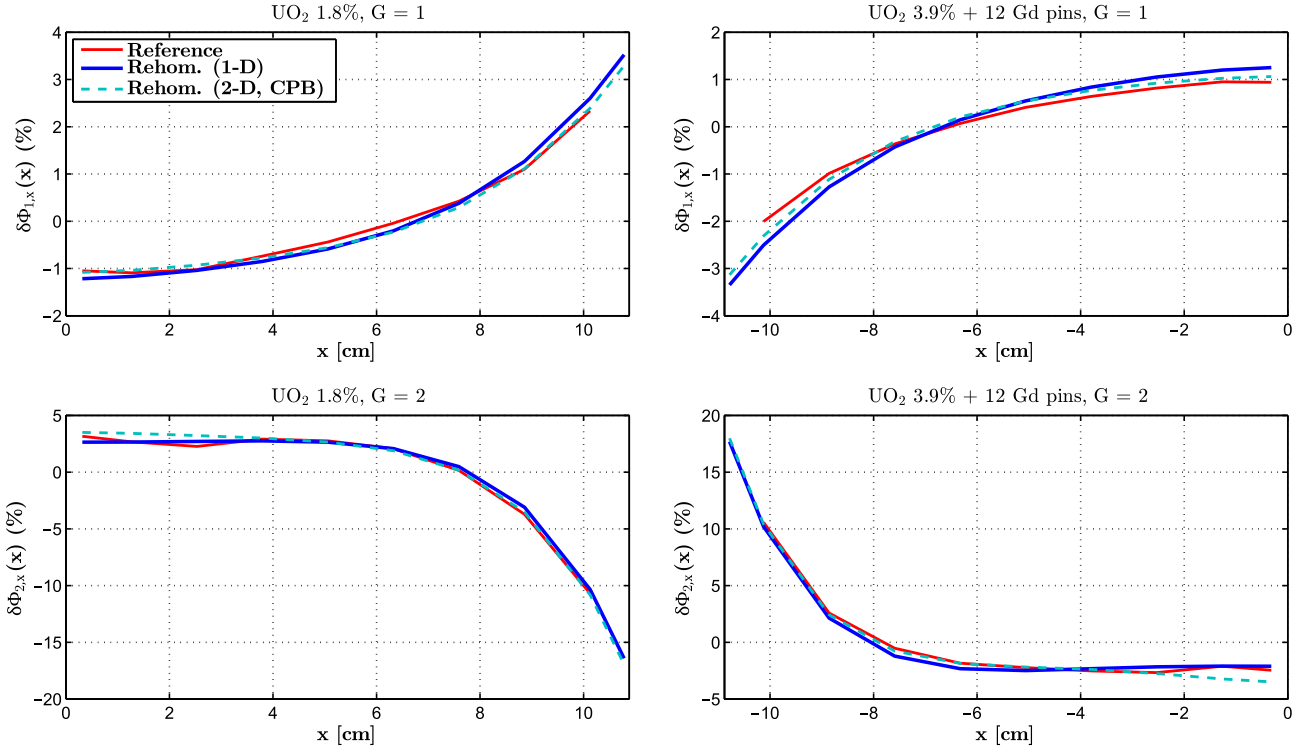

Fig. 20. Example 3: variation in the transverse-integrated flux distribution.

Table 7
Example 3: (a) number of non-linear flux iterations and errors in the integral parameters, and (b) errors in the absorption and production nodal cross sections.

(a)

Simulation	N_{iter}	Δk_{eff} [pcm]	UO_2 1.8% $\Delta\bar{P}_{fiss}$ (%)	UO_2 3.9% + 12 Gd pins $\Delta\bar{P}_{fiss}$ (%)
No rehom. (*a*)	9	757	−0.48 (0.58, −0.78)	0.33 (−0.34, 0.56)
2-D rehom. - CPB (*b*)	15	−105	0.24 (0.74, 0.11)	−0.16 (−0.43, −0.08)
2-D rehom. - MSS (*c*)	13	−136	0.41 (0.93, 0.28)	−0.28 (−0.54, −0.20)
1-D rehom. (*d*)	16	358	−0.37 (0.47, −0.60)	0.26 (−0.27, 0.43)

(b)

	UO_2 1.8%				UO_2 3.9% + 12 Gd pins			
	Errors (%)							
Simulation	$\Delta\Sigma_{a,1}$	$\Delta\Sigma_{a,2}$	$\Delta\nu\Sigma_{f,1}$	$\Delta\nu\Sigma_{f,2}$	$\Delta\Sigma_{a,1}$	$\Delta\Sigma_{a,2}$	$\Delta\nu\Sigma_{f,1}$	$\Delta\nu\Sigma_{f,2}$
No rehom. (*a*)	0.03	1.11	0.67	1.35	−0.11	−2.45	−0.48	−0.95
2-D rehom. - CPB (*b*)	0.07	0.98	0.73	1.10	−0.20	−0.88	−0.47	−1.23
2-D rehom. - MSS (*c*)	0.07	0.99	0.72	1.10	−0.19	−0.84	−0.46	−1.24
1-D rehom. (*d*)	0.07	0.99	0.73	1.10	−0.19	−1.62	−0.48	−0.97

Table 8
Example 3: errors in the absorption and production cross sections rehomogenized with the reference 2-D flux variation and with a least-squares best fit of it.

	UO_2 1.8%				UO_2 3.9% + 12 Gd pins			
	Errors (%)							
Flux variation (2-D)	$\Delta\Sigma_{a,1}$	$\Delta\Sigma_{a,2}$	$\Delta\nu\Sigma_{f,1}$	$\Delta\nu\Sigma_{f,2}$	$\Delta\Sigma_{a,1}$	$\Delta\Sigma_{a,2}$	$\Delta\nu\Sigma_{f,1}$	$\Delta\nu\Sigma_{f,2}$
Reference	0.08	0.89	0.74	0.91	−0.20	−1.27	−0.48	−0.86
Best fit	0.06	0.98	0.72	1.07	−0.18	−1.22	−0.47	−1.11

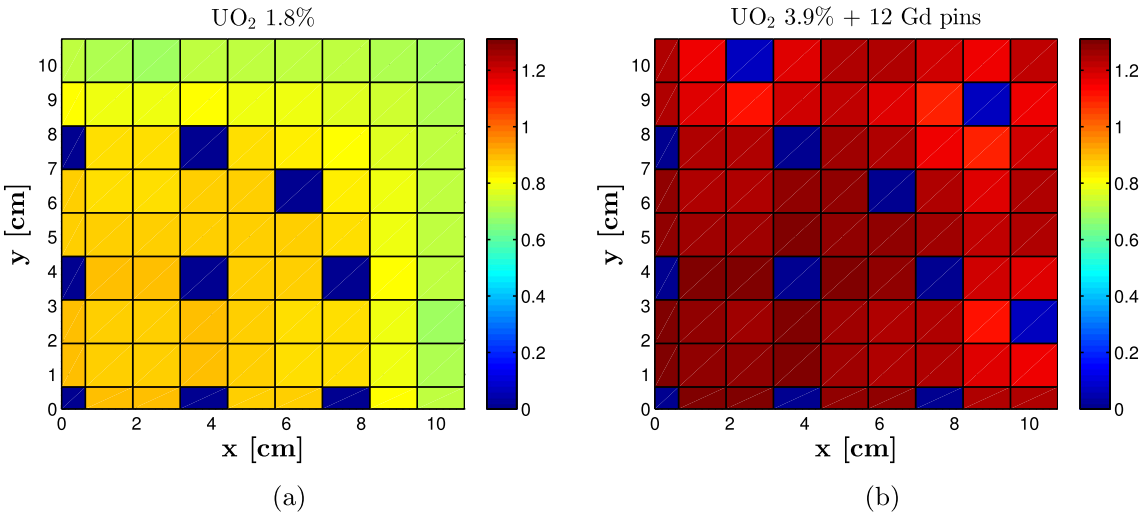

Fig. 21. Example 3: reference pin power (normalized to the colorset-averaged value) in the assemblies (a) without and (b) with gadolinium-bearing fuel pins.

leakage approximation. We have observed convergence to the same solution (in terms of k_{eff}, the nodal-flux distribution $\bar{\Phi}_G$, and the cross-section corrections $\delta\Sigma_{x,G}$) irrespective of the intranodal shape assumed for $L_{G,y}(x)$ and $L_{G,x}(y)$. This finding is related to the corrections on the assembly-surface discontinuity factors $\delta f_{G,d\pm}$ and can be explained as follows. The transverse-leakage approximation affects the nodal estimates of $\Phi^{hom}_{G,d\pm}$ and $J_{G,d\pm}$, which are input quantities to the spatial rehomogenization algorithm (see Section 2). However, the corrections $\delta f_{G,d\pm}$ vary in such a way that the modal coefficients of the flux spatial perturbation [Eq. (4)] converge to the same values obtained with other transverse-leakage approximations. Eventually, also the heterogeneous quantities $\left(f^{\infty}_{G,d\pm}+\delta f_{G,d\pm}\right)\Phi^{hom}_{G,d\pm}$ and $J_{G,d\pm}$ converge to the same values. The discontinuity-factor correction acts thus as a *free parameter* that enables convergence to the unique solution of the coupled nodal (i.e., CMFD + NEM) and rehomogenization fields.

For Example 1, Table 13 shows the corrections $\delta f_{G,d\pm}$ determined with calculation *b* and three different transverse-leakage distributions: the flat-leakage approximation (in which the intranodal shape is considered as uniform and equal to the node-averaged value of the transverse leakage), the standard three-node quadratic fit, and the quadratic shape from Eq. (43). The flat-leakage approximation leads to the highest variations in $\delta f_{G,d\pm}$, whereas Eq. (43) leads to the smallest.

The insensitivity to the transverse-leakage approach has also been observed with the 1-D rehomogenization. More investigation is needed to find a mathematical justification of this behavior.

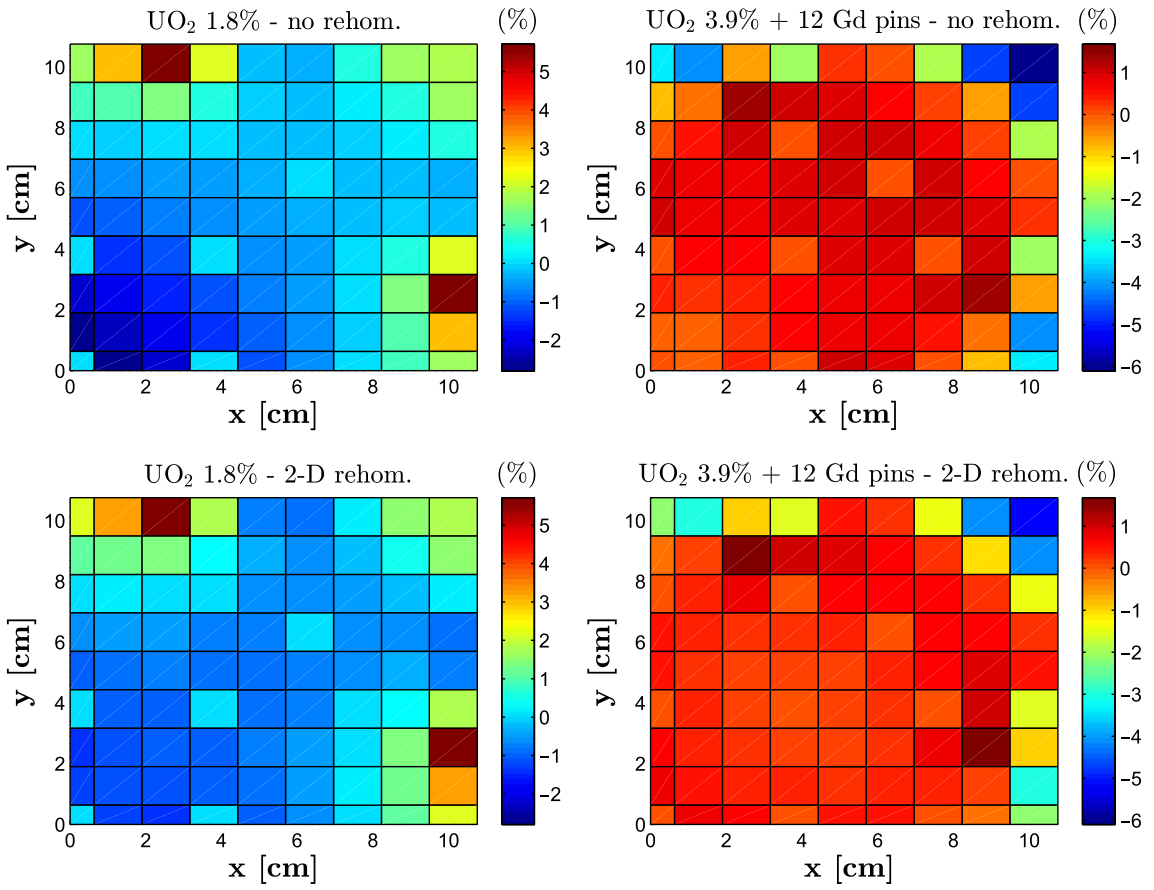

Fig. 22. Example 3: relative error (in percentage) in the pin-power distribution computed with calculations *a* and *b*.

Table 9
Example 3: RMS deviations (in percentage) in the pin-by-pin two-group flux and total fission power.

	UO_2 1.8%				UO_2 3.9% + 12 Gd pins			
Simulation	$RMS_{\Phi_1,r}$	$RMS_{\Phi_2,r}$	$RMS_{P,r}$	$RMS_{P,wa}$	$RMS_{\Phi_1,r}$	$RMS_{\Phi_2,r}$	$RMS_{P,r}$	$RMS_{P,wa}$
No rehom. (*a*)	0.37	1.24	1.55	1.05	0.51	1.38	1.61	2.11
2-D rehom. – CPB (*b*)	0.34	1.18	1.47	1.04	0.22	1.20	1.29	1.76
1-D rehom. (*d*)	0.34	1.23	1.56	1.03	0.34	1.23	1.42	1.86

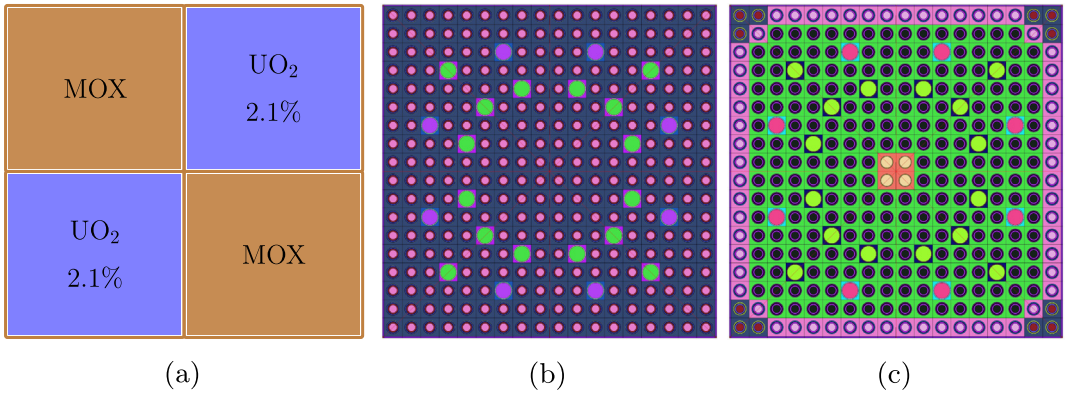

Fig. 23. (a) Assembly set of Example 4. Layout of the (b) UO_2 and (c) MOX fuel assemblies.

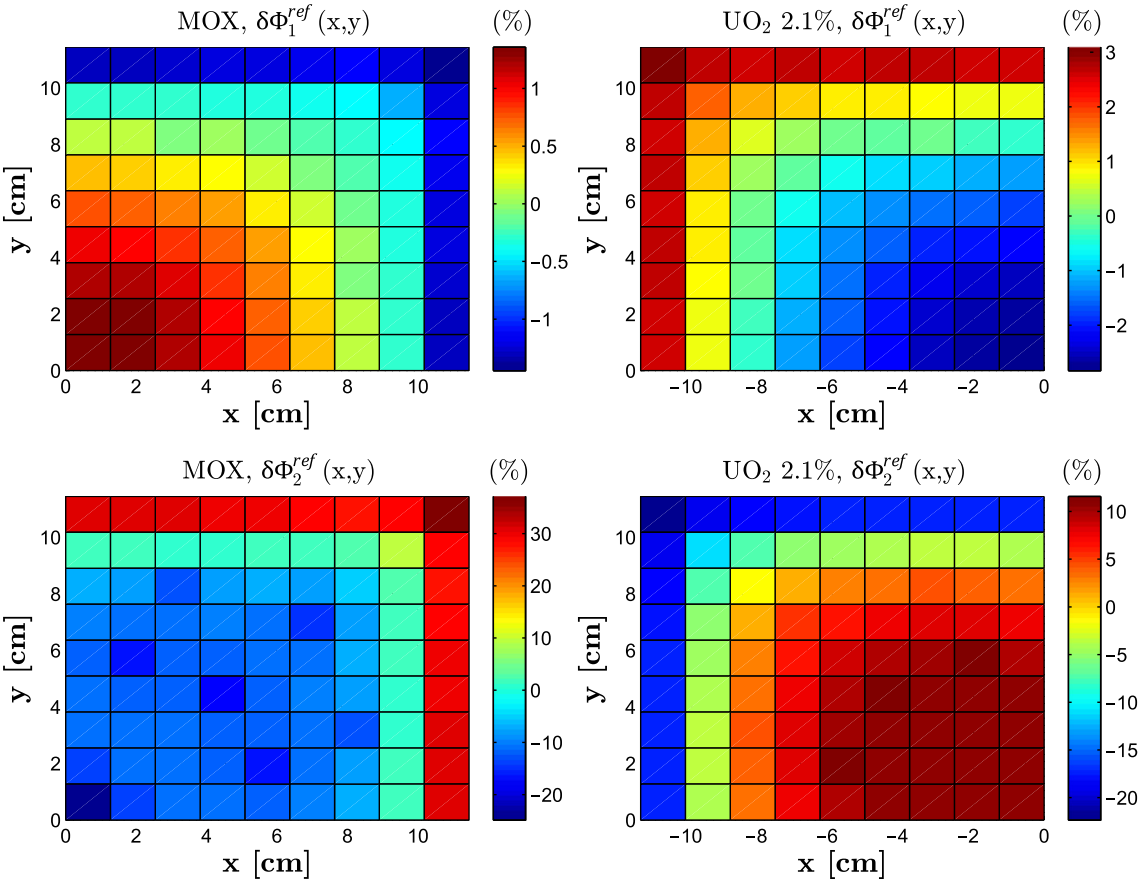

Fig. 24. Example 4: reference variation (in percentage) in the 2-D flux distribution.

4.2. Analysis on the discontinuity factors

In Section 3, we have only assessed the accuracy of the cross-section corrections. We now make a similar analysis on the discontinuity factors.

We evaluate the reference environmental discontinuity factors $f_{G,d\pm}^{\mathrm{env,ref}}$ with a nodal-equivalence approach applied to the colorset transport calculation. We define the homogeneous transverse-integrated neutron flux in the real environment with a quartic expansion, as in the conventional NEM equations:

$$\Phi_{G,d}^{\mathrm{hom,ref}}(u_d) = \bar{\Phi}_G^{\mathrm{ref}} + \sum_{i=1}^{4} a_{G,d,i}^{\mathrm{ref}} P_{G,i}(u_d), \tag{45}$$

where $\bar{\Phi}_G^{\mathrm{ref}}$ is the node-averaged flux from the reference transport simulation. The basis functions $P_{G,i}(u_d)$ are those defined in Eq. (5). The directional modal coefficients $a_{G,d,i}^{\mathrm{ref}}$ in a given node are determined with a linear system of four equations per group: (*i*) the conservation of the reference directional net current at the left boundary of the node ($J_{G,d-}^{\mathrm{ref}}$); (*ii*) the conservation of the reference directional net current at the right boundary of the node ($J_{G,d+}^{\mathrm{ref}}$); the projection of the transverse-integrated, two-group nodal diffusion equation in the environment over the (*iii*) first- and (*iv*) second-order NEM basis functions [Eqs. (5a) and (5b)].

We exploit the symmetry of the four-assembly configurations considered in this work and determine the reference surface-averaged currents with the two-group nodal balance in the colorset:

$$|J_{G,d\pm}^{\mathrm{ref}}| = \frac{\Delta d}{2}\left(\Sigma_{t,G}^{\mathrm{ref}}\bar{\Phi}_G^{\mathrm{ref}} - \frac{\chi_G^{\mathrm{ref}}}{k_{\mathrm{eff}}^{\mathrm{ref}}}\sum_{G'=1}^{2}\nu\Sigma_{f,G'}^{\mathrm{ref}}\bar{\Phi}_{G'}^{\mathrm{ref}} - \sum_{G'=1}^{2}\Sigma_{s,G'\to G}^{\mathrm{ref}}\bar{\Phi}_{G'}^{\mathrm{ref}}\right). \tag{46}$$

The cross sections in Eq. (46) have been condensed and homogenized with the neutron flux energy spectrum and spatial distribution of the colorset environment.

The j^{th}-order (with j = 1, 2) 1-D homogeneous equation is

$$\int_{-1/2}^{1/2} du_d P_j(u_d)\left[\frac{dJ_{G,d}^{\mathrm{ref}}(u_d)}{du_d} + \Sigma_{t,G}^{\mathrm{ref}}\Phi_{G,d}^{\mathrm{hom,ref}}(u_d) - S_{G,d}^{\mathrm{ref}}(u_d)\right] = 0, \tag{47}$$

where the source term $S_{G,d}^{\mathrm{ref}}(u_d)$ includes the scattering and fission operators and the transverse leakage:

$$S_{G,d}^{\mathrm{ref}}(u_d) = \frac{\chi_G^{\mathrm{ref}}}{k_{\mathrm{eff}}^{\mathrm{ref}}}\sum_{G'=1}^{2}\nu\Sigma_{f,G'}^{\mathrm{ref}}\Phi_{G',d}^{\mathrm{hom,ref}}(u_d) + \sum_{G'=1}^{2}\Sigma_{s,G'\to G}^{\mathrm{ref}}\Phi_{G',d}^{\mathrm{hom,ref}}(u_d) - L_{G,t}(u_d). \tag{48}$$

In Eq. (48), the transverse leakage $L_{G,t}(u_d)$ is approximated with the conventional quadratic fit over the node under consideration and the two adjacent nodes along the direction *d*. The leakage expansion coefficients are computed preserving the reference volume-averaged transverse leakage $\bar{L}_{G,t}^{\mathrm{ref}}$ (evaluated with Eq. (46)) in the three nodes.

After solving for the modal coefficients $a_{G,d,i}^{\mathrm{ref}}$, the reference discontinuity factor is estimated as

$$f_{G,d\pm}^{\mathrm{env,ref}} = \frac{\Phi_{G,d\pm}^{\mathrm{het,ref}}}{\Phi_{G,d}^{\mathrm{hom,ref}}\left(\pm\frac{1}{2}\right)}, \tag{49}$$

where $\Phi_{G,d\pm}^{\mathrm{het,ref}}$ is the heterogeneous surface-averaged flux from the reference transport calculation. Since this quantity is not among the edits of APOLLO2-A, we make the following assumption:

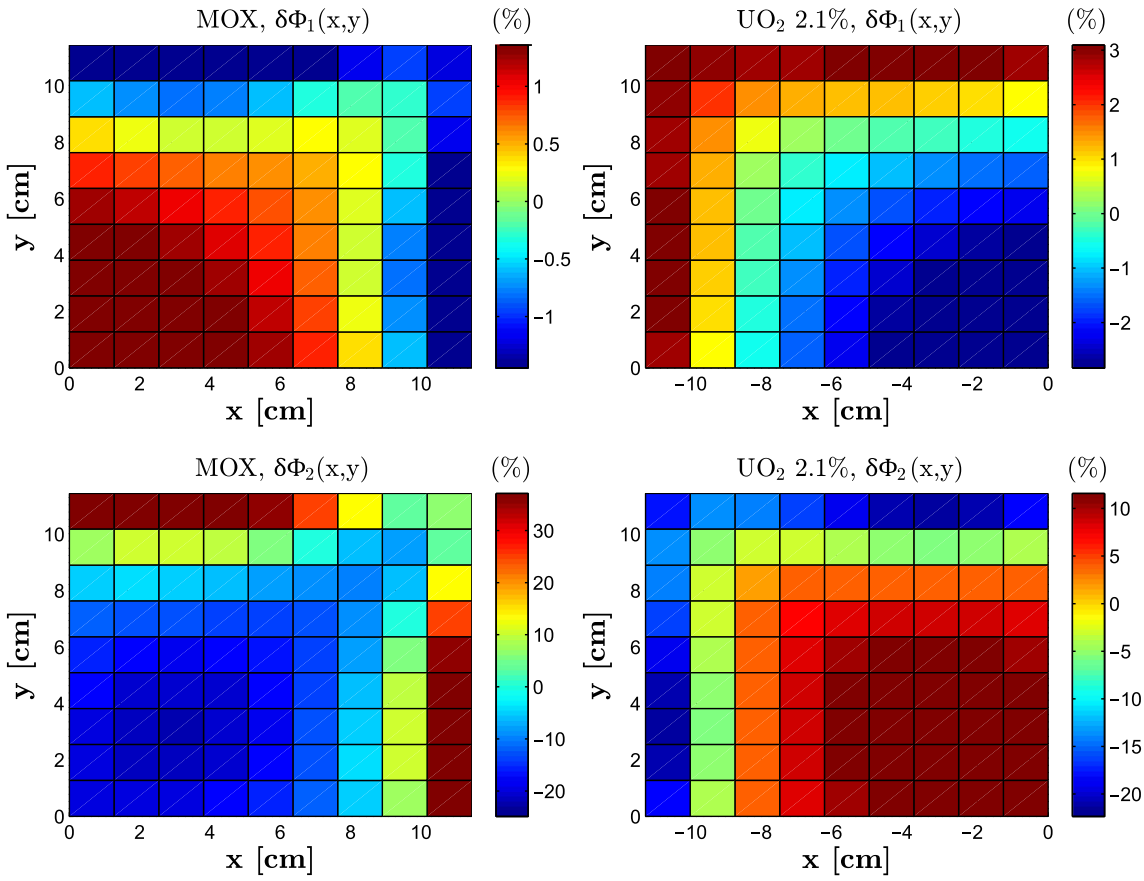

Fig. 25. Example 4: variation (in percentage) in the 2-D flux distribution, as computed with the CPB-based 2-D rehomogenization.

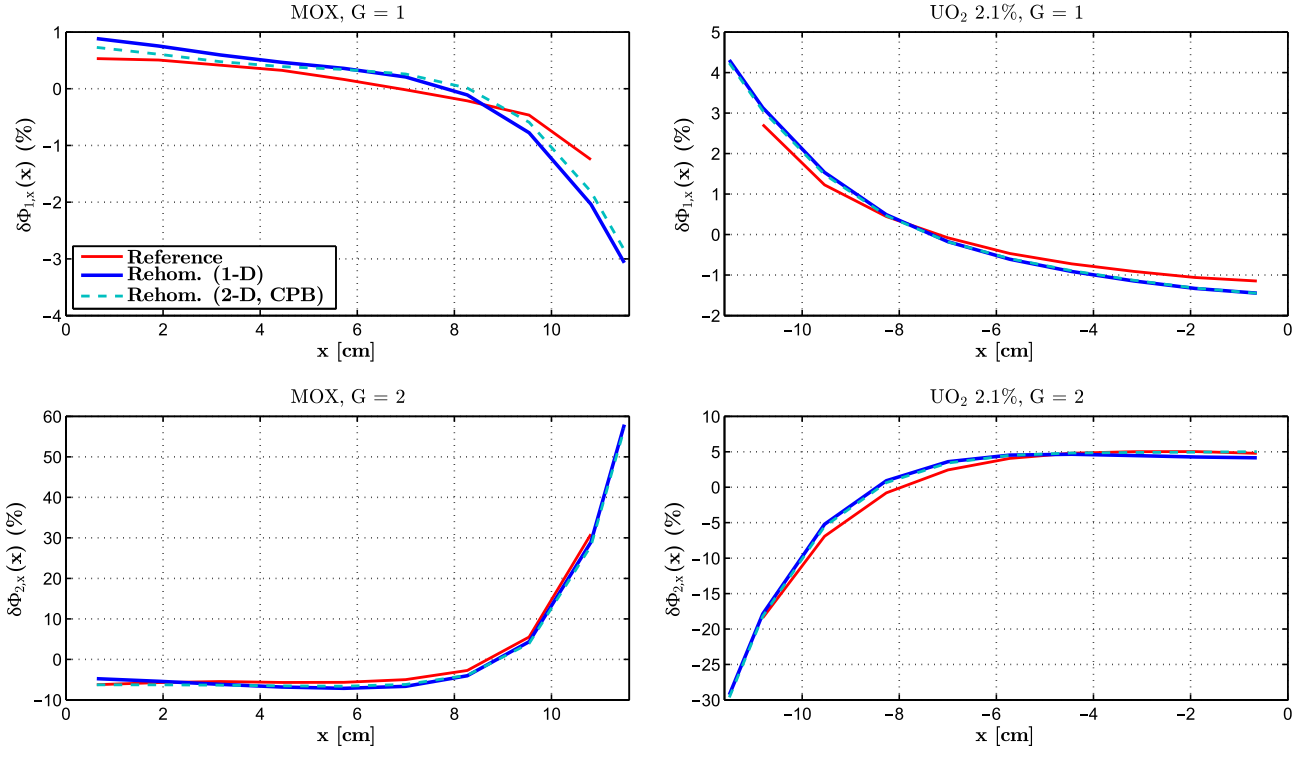

Fig. 26. Example 4: variation in the transverse-integrated flux distribution.

Table 10
Example 4: (a) number of non-linear flux iterations and errors in the integral parameters, and (b) errors in the absorption and production nodal cross sections.

(a)

Simulation	N_{iter}	Δk_{eff} [pcm]	UO_2 2.1% $\Delta\overline{P}_{\text{fiss}}$ (%)	MOX $\Delta\overline{P}_{\text{fiss}}$ (%)
No rehom. (*a*)	11	199	1.94 (0.81, 2.24)	−1.44 (−0.46, −1.86)
2-D rehom. – CPB (*b*)	29	276	0.38 (0.70, 0.22)	−0.28 (−0.39, −0.19)
2-D rehom. – MSS (*c*)	17	273	0.48 (0.89, 0.29)	−0.36 (−0.50, −0.24)
1-D rehom. (*d*)	17	286	0.22 (0.48, 0.10)	−0.17 (−0.27, −0.09)

(b)

	UO_2 2.1%				MOX			
	Errors (%)							
Simulation	$\Delta\Sigma_{a,1}$	$\Delta\Sigma_{a,2}$	$\Delta\nu\Sigma_{f,1}$	$\Delta\nu\Sigma_{f,2}$	$\Delta\Sigma_{a,1}$	$\Delta\Sigma_{a,2}$	$\Delta\nu\Sigma_{f,1}$	$\Delta\nu\Sigma_{f,2}$
No rehom. (*a*)	0.54	1.18	0.61	1.35	−1.05	0.31	−0.52	0.45
2-D rehom. - CPB (*b*)	0.54	1.17	0.62	1.31	−1.01	−1.28	−0.43	−1.40
2-D rehom. - MSS (*c*)	0.55	1.16	0.62	1.30	−1.0	−1.27	−0.44	−1.39
1-D rehom. (*d*)	0.54	1.16	0.62	1.29	−1.0	−1.19	−0.41	−1.30

Table 11
Example 4: errors in the absorption and production cross sections rehomogenized with the reference 2-D flux variation and with a least-squares best fit of it.

	UO_2 2.1%				MOX			
	Errors (%)							
Flux variation (2-D)	$\Delta\Sigma_{a,1}$	$\Delta\Sigma_{a,2}$	$\Delta\nu\Sigma_{f,1}$	$\Delta\nu\Sigma_{f,2}$	$\Delta\Sigma_{a,1}$	$\Delta\Sigma_{a,2}$	$\Delta\nu\Sigma_{f,1}$	$\Delta\nu\Sigma_{f,2}$
Reference	0.59	0.88	0.68	0.68	−1.05	−0.06	−0.49	0.07
Best fit	0.55	1.11	0.63	1.17	−1.04	−0.71	−0.48	−0.74

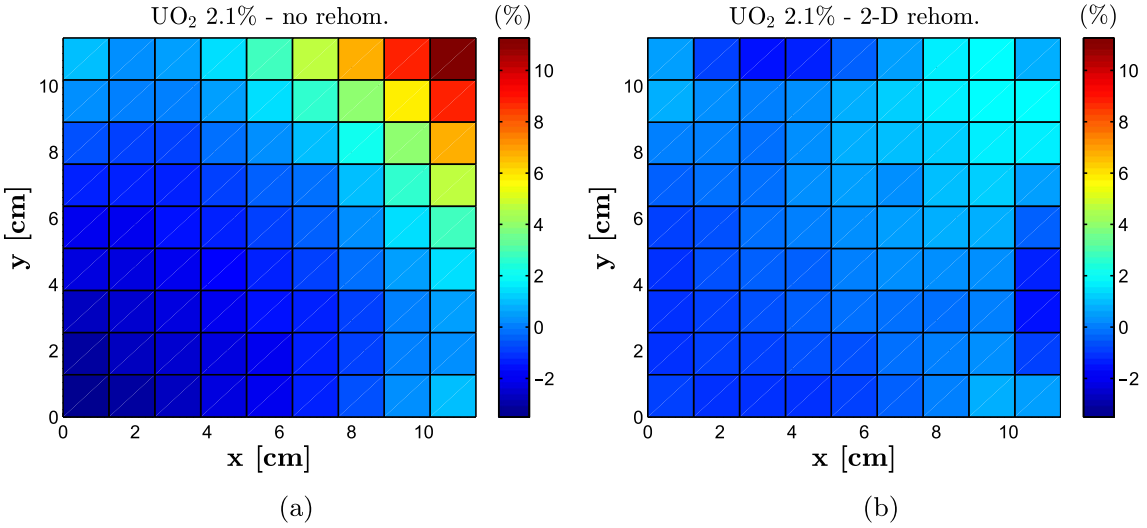

Fig. 27. Example 4: relative error (in percentage) in the pin-by-pin thermal flux in the UO_2 assembly. The plots refer to the calculations (a) without rehomogenization and (b) with the CPB-based 2-D rehomogenization.

$$\Phi^{\text{het,ref}}_{G,d\pm} \approx \Phi^{\text{ref}}_{G,\text{wg}}, \tag{50}$$

where $\Phi^{\text{ref}}_{G,\text{wg}}$ denotes the spatially averaged value of the water-gap flux from the reference calculation.

Table 14 reports the relative differences (in percentage) between the discontinuity-factor estimates of calculations *a*, *b* and *d* and the reference values determined with Eq. (49). The improvement in the discontinuity factors is less apparent than that observed in the cross sections in Section 3. In particular, in the UO_2 and MOX assemblies of Example 4 (Table 14(d)) the corrected values have significantly higher errors than the infinite-medium ones. We remark that the reference quantities in Eqs. (46)–(49) (cross sections, node-averaged fluxes, surface-averaged fluxes and currents) come from the solution of the 281-group transport equation in the real environment, with successive collapsing to two groups. These quantities incorporate not only the spatial effects of the environment but also the spectral ones, which are not taken into account by spatial rehomogenization. The discontinuity factors computed with Eq. (49), which we consider here as reference values, are therefore not fully consistent with our spatial rehomogenization approach. A more rigorous assessment should be made computing them with a reference solution that excludes the spectral effects (namely, solving the transport equation in the colorset environment directly in a two-group structure, without energy condensation).

To conclude the analysis on the discontinuity factors, we assess the impact of the reference $\delta f_{G,d\pm}$ on the nodal estimates of the

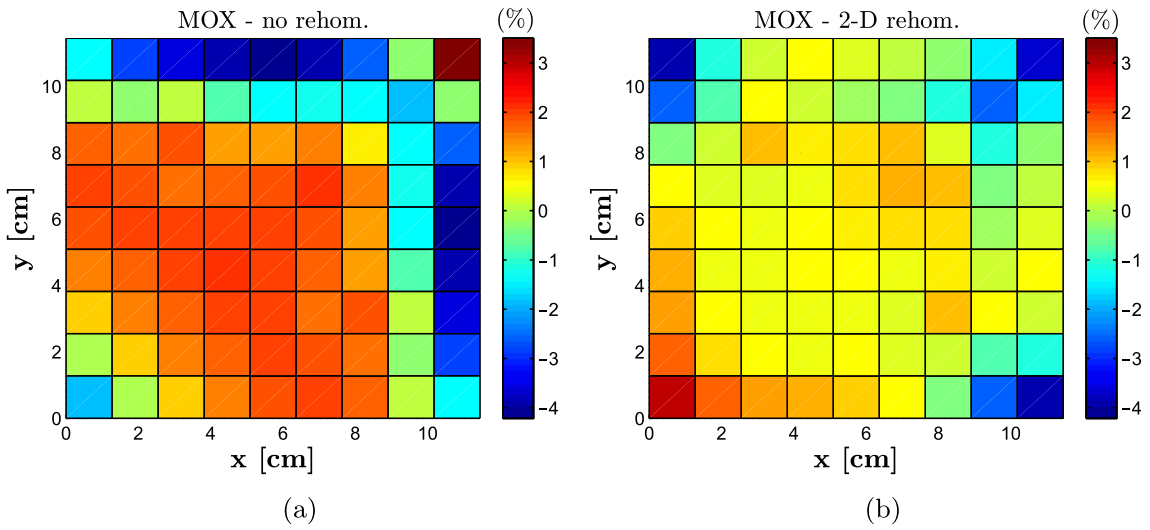

Fig. 28. Example 4: relative error (in percentage) in the pin-by-pin thermal flux in the MOX assembly. The plots refer to the calculations (a) without rehomogenization and (b) with the CPB-based 2-D rehomogenization.

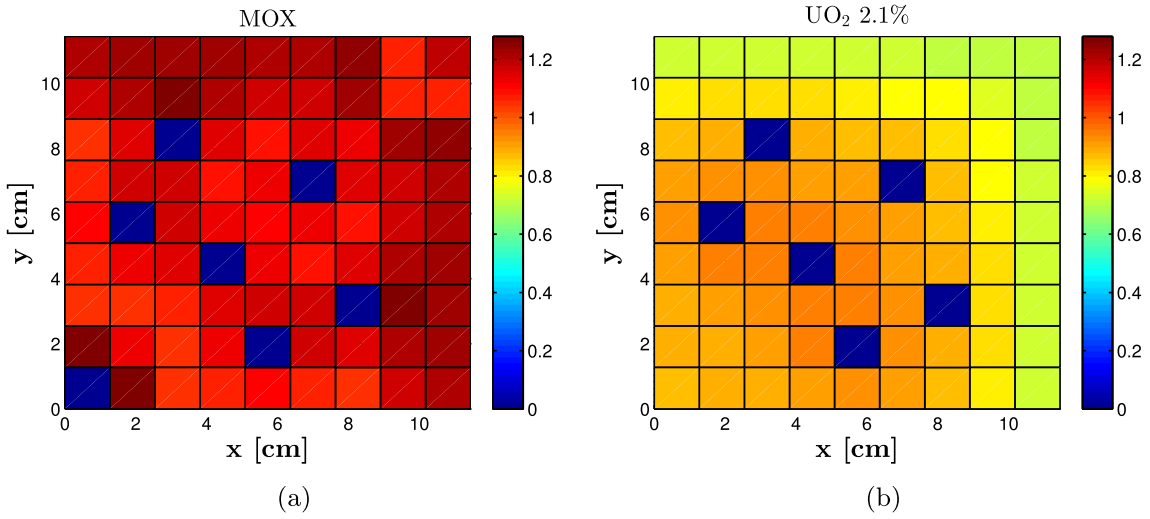

Fig. 29. Example 4: reference pin power (normalized to the colorset-averaged value) in the (a) MOX and (b) UO_2 assemblies.

multiplication factor and fission power. For this purpose, we run two nodal calculations with the cross sections rehomogenized by the reference 2-D flux variation (see Tables 2, 5, 8 and 11). The first of these uses the infinite-medium discontinuity factors $f^{\infty}_{G,d\pm}$, whereas the second uses the reference discontinuity factors $f^{\text{env,ref}}_{G,d\pm}$ from Eq. (49). The results are shown in Table 15. Whilst the discontinuity-factor corrections have a mild impact on the nodal simulations of Examples 1 and 4, their effect is substantial in Examples 2 and 3. Comparing the errors in k_{eff} and $\overline{P}_{\text{fiss}}$ shown in Table 15 with those resulting from rehomogenization (Tables 1, 4, 7 and 10), the following conclusions can be drawn for the various test cases:

- In Example 1, both the 1-D and 2-D models overestimate the corrections on k_{eff} and on the fission power (especially the 2-D one).
- In Example 2, similar considerations apply to the 2-D model, whereas the 1-D approach provides a very accurate result.
- In Example 3, the correction on k_{eff} is overestimated with the 2-D model and underestimated with the 1-D one; both approaches underestimate the corrections on $\overline{P}_{\text{fiss}}$ (particularly the 1-D model).
- In Example 4, the computed corrections on k_{eff} and $\overline{P}_{\text{fiss}}$ go in the wrong direction. The spatial effects have negligible impact on the assembly-averaged fission power.

4.3. Numerical features and implementation

As spectral rehomogenization, spatial rehomogenization also translates into an additional level of feedback in the global core calculation (Gamarino et al., 2018a). In a two-group framework with four basis functions per direction and four cross terms (see Section 2), the rank of the 2-D rehomogenization linear system is 32. Since the rehomogenization problem is solved independently in each node after updating the corner-point flux distribution [Eq. (23) or (28)], the corresponding computational cost can be mitigated via parallelization of the algorithm.

In the present work, the rehomogenization coefficients [Eqs. (32 and (34)] have been computed post-processing the APOLLO2-A single-assembly cell-homogenized cross sections and flux distribution. Better modeling may be achieved incorporating their calculation into the lattice-code routines, thus accounting for within-cell heterogeneity. As in the case of spectral rehomogenization, an

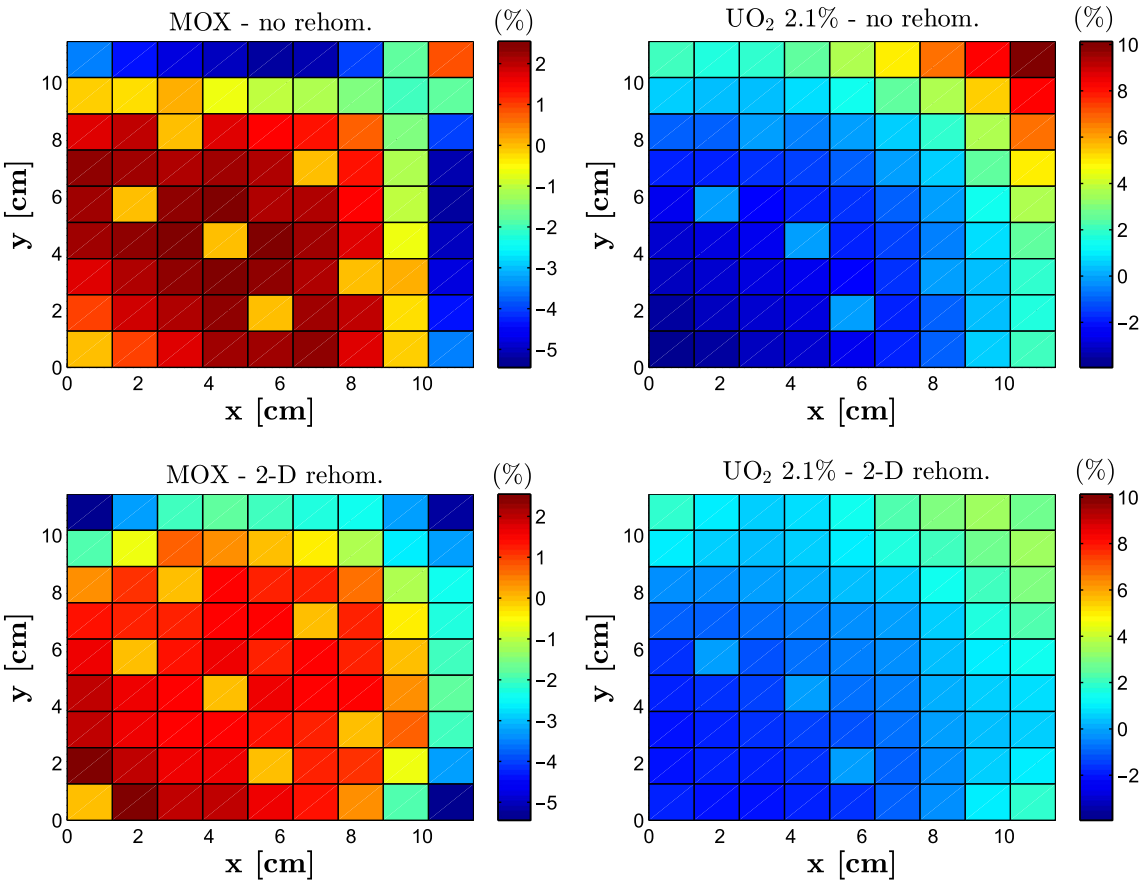

Fig. 30. Example 4: relative error (in percentage) in the pin-power distribution computed with calculations *a* and *b*.

Table 12
Example 4: RMS deviations (in percentage) in the pin-by-pin two-group flux and total fission power.

	UO_2 2.1%				MOX			
Simulation	$RMS_{\Phi_1,r}$	$RMS_{\Phi_2,r}$	$RMS_{P,r}$	$RMS_{P,wa}$	$RMS_{\Phi_1,r}$	$RMS_{\Phi_2,r}$	$RMS_{P,r}$	$RMS_{P,wa}$
No rehom. (*a*)	0.35	3.0	3.1	2.68	0.73	2.10	2.59	4.09
2-D rehom. - CPB (*b*)	0.45	0.89	1.51	1.21	0.70	1.25	1.97	2.64
1-D rehom. (*d*)	0.45	2.40	2.48	1.73	0.77	1.17	1.86	2.50

approximation is made in the formulation of the weighted-residual equations [Eq. (37)]. Eq. (30) is valid in the real environment, whereas in practice we use the pin-by-pin cross sections of the infinite medium. In order to verify the impact of this approximation, we have repeated the calculations of Section 3 computing the rehomogenization coefficients of Eq. (32) with the colorset cell-homogenized cross sections. For Examples 2 and 4, Table 16 shows the errors of calculation *b* with these improved rehomogenization parameters. Comparing Tables 16(a) and 4, we observe that the differences in the results are negligible in the colorset with control rods. In the UO_2/MOX colorset (Tables 16(b) and 10), the differences are more tangible. Whilst the error in k_{eff} increases of about 40 pcm compared to the case with standard rehomogenization coefficients (i.e., computed with the infinite-medium pin-by-pin cross sections), the errors in the fission power are halved. However, in both cases the power errors are significantly smaller than those of calculation *a*. Moreover, the improvement in the nodal cross sections of the MOX assembly observed with the environmental coefficients is small if compared to the reference estimates (see Table 11). We have verified that the impact of the aforementioned approximation on the rehomogenization parameters is marginal also in the test cases with Pyrex rods and gadolinium-bearing fuel pins. It can therefore be concluded that using the infinite-medium fine-mesh cross sections in Eq. (32) does not significantly affect the performance of the method. Intranodal depletion effects can be easily incorporated into the rehomogenization coefficients via the conventional within-assembly cross-section polynomial expansions (Wagner et al., 1981; Forslund et al., 2001).

The memory requirement for the storage of the rehomogenization parameters in the cross-section libraries is minimized exploiting the symmetry of the fuel-assembly internal layout. These additional coefficients are only computed and stored for an assembly quarter. During the nodal calculation, their sign is determined based on the orientation of the node within the fuel assembly.

As observed for spectral rehomogenization (Gamarino et al., 2018a), convergence of the algorithm benefits from under-relaxation, which dampens numerical oscillations. Convergence difficulties have never been encountered. Except for the CPB approach in the UO_2/MOX benchmark problem (Table 10), the increase in the number of power iterations of the eigenvalue

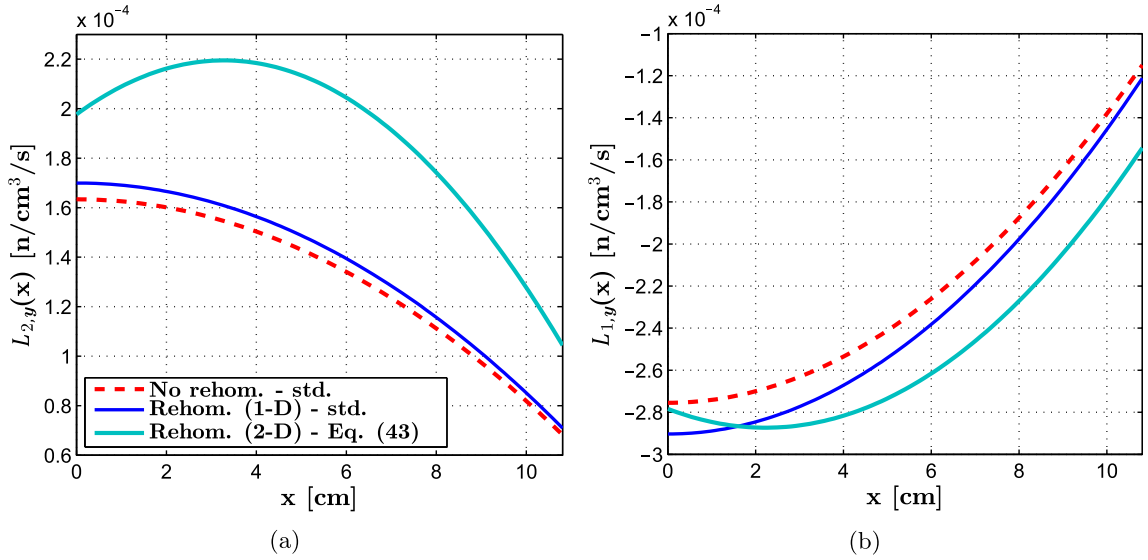

Fig. 31. (a) Thermal- and (b) fast-group transverse-leakage distributions in the 1.8%-enriched UO_2 assembly of Example 1. The abbreviation 'std.' stands for 'standard' and refers to the three-node quadratic fit. In both groups, the curves are normalized to the node-averaged transverse leakage from the nodal calculation. Units are in [neutrons/(cubic centimeter · second)].

Table 13
Example 1: corrections (in percentage) on the assembly-surface discontinuity factors computed with calculation *b* and different transverse-leakage approximations.

	UO_2 1.8%		UO_2 3.1% + 16 b.p. rods	
Leakage approximation	δf_1 (%)	δf_2 (%)	δf_1 (%)	δf_2 (%)
Flat	−0.15	1.64	0.21	−2.87
Quadratic (standard)	0.05	0.44	0.03	−1.87
Quadratic (2-D rehom.)	−0.04	0.23	0.12	−1.70

Table 14
Relative differences (in percentage) between the environmental assembly discontinuity factors computed with rehomogenization and with a nodal equivalence applied to the reference data from APOLLO2-A.

(a)

Example 1	UO_2 1.8%		UO_2 3.1% + 16 b.p. rods	
Simulation	Δf_1^{env} (%)	Δf_2^{env} (%)	Δf_1^{env} (%)	Δf_2^{env} (%)
No rehom. (*a*)	0.11	1.41	0.68	−0.69
2-D rehom. – CPB (*b*)	0.07	1.64	0.80	−2.38
1-D rehom. (*d*)	0.08	1.72	0.83	−2.15

(b)

Example 2	UO_2 1.8%		UO_2 2.4% + 24 AIC rods	
Simulation	Δf_1^{env} (%)	Δf_2^{env} (%)	Δf_1^{env} (%)	Δf_2^{env} (%)
No rehom. (*a*)	0.14	0.10	0.81	3.52
2-D rehom. - CPB (*b*)	0.12	0.36	0.33	−1.68
1-D rehom. (*d*)	0.13	0.44	0.55	−0.56

(c)

Example 3	UO_2 1.8%		UO_2 3.9% + 12 Gd pins	
Simulation	Δf_1^{env} (%)	Δf_2^{env} (%)	Δf_1^{env} (%)	Δf_2^{env} (%)
No rehom. (*a*)	0.41	2.95	0.66	−4.47
2-D rehom. – CPB (*b*)	0.31	2.97	0.27	−4.14
1-D rehom. (*d*)	0.34	3.22	0.22	−4.18

(d)

Example 4	UO_2 2.1%		MOX	
Simulation	Δf_1^{env} (%)	Δf_2^{env} (%)	Δf_1^{env} (%)	Δf_2^{env} (%)
No rehom. (*a*)	0.23	5.90	0.34	2.86
2-D rehom. – CPB (*b*)	0.21	8.76	0.33	−10.7
1-D rehom. (*d*)	0.21	8.71	0.24	−9.86

Table 15
Errors in the multiplication factor and assembly-averaged fission power estimated with the reference spatial cross-section corrections ($\delta\Sigma_{r,G}^{\text{spat,ref}}$) and the infinite-medium ($f_{G,d\pm}^{\infty}$) or reference ($f_{G,d\pm}^{\text{env,ref}}$) discontinuity factors.

(a)

Example 1		UO_2 1.8%	UO_2 3.1% + 16 b.p. rods
	Δk_{eff} [pcm]	$\Delta\overline{P}_{\text{fiss}}$ (%)	$\Delta\overline{P}_{\text{fiss}}$ (%)
$\delta\Sigma_{r,G}^{\text{spat,ref}}$, $f_{G,d\pm}^{\infty}$	−36	0.51 (0.81, 0.43)	−0.43 (−0.57, −0.39)
$\delta\Sigma_{r,G}^{\text{spat,ref}}$, $f_{G,d\pm}^{\text{env,ref}}$	−43	0.65 (0.54, 0.68)	−0.55 (−0.38, −0.61)

(b)

Example 2		UO_2 1.8%	UO_2 2.4% + 24 AIC rods
	Δk_{eff} [pcm]	$\Delta\overline{P}_{\text{fiss}}$ (%)	$\Delta\overline{P}_{\text{fiss}}$ (%)
$\delta\Sigma_{r,G}^{\text{spat,ref}}$, $f_{G,d\pm}^{\infty}$	−33	0.76 (0.38, 0.84)	−0.97 (−0.36, −1.15)
$\delta\Sigma_{r,G}^{\text{spat,ref}}$, $f_{G,d\pm}^{\text{env,ref}}$	−141	0.07 (−0.03, 0.095)	−0.09 (0.02, −0.13)

(c)

Example 3		UO_2 1.8%	UO_2 3.9% + 12 Gd pins
	Δk_{eff} [pcm]	$\Delta\overline{P}_{\text{fiss}}$ (%)	$\Delta\overline{P}_{\text{fiss}}$ (%)
$\delta\Sigma_{r,G}^{\text{spat,ref}}$, $f_{G,d\pm}^{\infty}$	210	−0.24 (0.71, −0.50)	0.17 (−0.42, 0.36)
$\delta\Sigma_{r,G}^{\text{spat,ref}}$, $f_{G,d\pm}^{\text{env,ref}}$	137	0.95 (0.74, 1.0)	−0.65 (−0.43, −0.72)

(d)

Example 4		UO_2 2.1%	MOX
	Δk_{eff} [pcm]	$\Delta\overline{P}_{\text{fiss}}$ (%)	$\Delta\overline{P}_{\text{fiss}}$ (%)
$\delta\Sigma_{r,G}^{\text{spat,ref}}$, $f_{G,d\pm}^{\infty}$	97	1.70 (0.76, 1.96)	−1.27 (−0.43, −1.62)
$\delta\Sigma_{r,G}^{\text{spat,ref}}$, $f_{G,d\pm}^{\text{env,ref}}$	61	2.01 (0.74, 2.37)	−1.49 (−0.42, −1.96)

calculation is below a factor of 1.8 and, therefore, acceptable. In coupled calculations (namely, with thermal feedback), the additional level of non-linearity introduced by the cross-section and discontinuity-factor updates would be nested in the thermal-hydraulic iterations, thus alleviating the observed increase in the number of power iterations and computing time.

To conclude, the 2-D rehomogenization method presented in this work can also be viewed as an original dehomogenization approach. If Eq. (2) is used, the assumption is made that the 2-D flux variation is a smooth function of the x and y coordinates and is not affected by intranodal heterogeneity. The impact of this approximation on the reconstruction of the pin-by-pin flux and power distributions should be assessed. A successful application of the 2-D rehomogenization for assembly dehomogenization as well would increase the attractiveness of the method and largely compensate for its higher computational cost compared to the 1-D model.

4.4. Complementarity between the spatial and spectral effects of the environment

We briefly address the complementarity of the various environmental effects on the nodal cross sections. For the benchmark problems analyzed in Section 3, Table 17 shows: (*i*) the reference spectral corrections $\delta\Sigma_{r,G}^{\text{spec,ref}}$, computed with the reference spectrum variation (Gamarino et al., 2018a; Gamarino et al., 2018b); (*ii*) the reference spatial corrections $\delta\Sigma_{r,G}^{\text{spat,ref}}$, computed with the reference 2-D flux spatial change; and (*iii*) the cross (i.e., mixed energy-space) corrections $\delta\Sigma_{r,G}^{\text{cross}}$, which have been estimated as

$$\delta\Sigma_{r,G}^{\text{cross}} = \Sigma_{r,G}^{\text{ref}} - \Sigma_{r,G}^{\infty} - \delta\Sigma_{r,G}^{\text{spec,ref}} - \delta\Sigma_{r,G}^{\text{spat,ref}}, \tag{51}$$

where $\Sigma_{r,G}^{\text{ref}}$ is the cross section condensed and homogenized in the colorset configuration, thus taking into account the global environmental effect. Even if the cross corrections are generally smaller than the spectral and spatial ones, they are not negligible, especially in the assemblies with the strongest heterogeneity. In particular, in the MOX assembly of Example 4 [Table 17(d)], the thermal absorption and production cross terms have magnitude comparable to or larger than the spectral and spatial ones, which have opposite sign and roughly cancel each other. One of the reasons of this behavior is that the flux spectrum deformation varies significantly with the distance from the assembly outer edge, whereas the correction $\delta\Sigma_{r,G}^{\text{spec,ref}}$ is computed with an average deformation in the assembly (Gamarino et al., 2018a). Taking into account the cross corrections is therefore important for an accurate prediction of the global cross-section variation.

From Table 17, some general features of the cross-section corrections can be observed:

- The spatial effects are only relevant in the thermal group, whereas the spectral ones are significant in both energy groups. There is no clear pattern for cross effects.
- In the heterogeneous assemblies, the sign and magnitude of the spatial corrections depend on the position of the main sources of heterogeneity within the fuel bundle.

Separating the various effects on the discontinuity factors is not equally straightforward for the reasons discussed in Section 4.2.

5. Conclusions

In this paper, we have developed a first-principle modal method to estimate the variation in the 2-D few-group flux distribution between the core environment and the infinite lattice. This method relaxes the main approximations of the original 1-D transverse-integrated rehomogenization.

Numerical results show that the errors in the multiplication factor and assembly-averaged fission power significantly decrease compared to the calculation with infinite-medium homogenization parameters. The cross-section corrections computed by the 2-D model always go in the right direction. In most cases they match the corrections determined with a least-squares best fit of the reference flux change, but they are higher than the reference values. One of the reasons of this outcome is that the polynomial and hyperbolic basis functions used for the modal expansion cannot

Table 16
Results of the CPB-based 2-D rehomogenization with environmental rehomogenization coefficients (i.e., computed with the colorset pin-by-pin cross sections).

(a)

Example 2	UO_2 1.8%			UO_2 2.4% + 24 AIC rods		
Δk_{eff} [pcm]	$\Delta\overline{P}_{\text{fiss}}$ (%)	$\Delta\Sigma_{a,2}$ (%)	$\Delta\nu\Sigma_{f,2}$ (%)	$\Delta\overline{P}_{\text{fiss}}$ (%)	$\Delta\Sigma_{a,2}$ (%)	$\Delta\nu\Sigma_{f,2}$ (%)
−32	−0.76 (−0.37,−0.84)	0.57	0.61	0.97 (0.36,1.14)	−1.34	−0.94

(b)

Example 4	UO_2 2.1%			MOX		
Δk_{eff} [pcm]	$\Delta\overline{P}_{\text{fiss}}$ (%)	$\Delta\Sigma_{a,2}$ (%)	$\Delta\nu\Sigma_{f,2}$ (%)	$\Delta\overline{P}_{\text{fiss}}$ (%)	$\Delta\Sigma_{a,2}$ (%)	$\Delta\nu\Sigma_{f,2}$ (%)
317	0.19 (0.66,−0.001)	1.27	1.44	−0.14 (−0.38,0.001)	−1.08	−1.18

Table 17
Cross-section changes due to the various types of environmental effects: spectral, spatial, and cross (i.e., mixed energy-space). The variations have been computed with respect to the infinite-medium values by using the reference data from APOLLO2-A.

(a)

Example 1	UO_2 1.8%					UO_2 3.1% + 16 b.p. rods				
	Variation (%)									
Type of effect	$\delta\Sigma_{a,1}$	$\delta\Sigma_{a,2}$	$\delta\nu\Sigma_{f,1}$	$\delta\nu\Sigma_{f,2}$	$\delta\Sigma_{s,1\to2}$	$\delta\Sigma_{a,1}$	$\delta\Sigma_{a,2}$	$\delta\nu\Sigma_{f,1}$	$\delta\nu\Sigma_{f,2}$	$\delta\Sigma_{s,1\to2}$
Spectral	0.074	−0.55	−0.34	−0.57	−0.58	−0.13	0.77	0.19	0.84	0.45
Spatial	0.028	−0.16	0.034	−0.30	−0.025	−0.007	−0.18	−0.026	0.33	0.005
Cross	−0.065	0.025	−0.15	0.067	0.045	0.034	−0.090	0.12	−0.12	−0.017
Global	0.037	−0.69	−0.46	−0.80	−0.56	−0.10	0.50	0.28	1.04	0.44

(b)

Example 2	UO_2 1.8%					UO_2 2.4% + 24 AIC rods				
	Variation (%)									
Type of effect	$\delta\Sigma_{a,1}$	$\delta\Sigma_{a,2}$	$\delta\nu\Sigma_{f,1}$	$\delta\nu\Sigma_{f,2}$	$\delta\Sigma_{s,1\to2}$	$\delta\Sigma_{a,1}$	$\delta\Sigma_{a,2}$	$\delta\nu\Sigma_{f,1}$	$\delta\nu\Sigma_{f,2}$	$\delta\Sigma_{s,1\to2}$
Spectral	0.78	−0.44	0.056	−0.46	0.61	−0.96	0.82	−0.23	1.12	−0.53
Spatial	−0.09	−0.31	−0.10	−0.39	0.072	−0.23	−1.24	0.13	0.41	0.062
Cross	0.034	0.098	−0.008	0.13	−0.043	−0.10	−0.20	−0.048	−0.29	−0.026
Global	0.72	−0.65	−0.055	−0.72	0.64	−1.29	−0.62	−0.15	1.23	−0.49

(c)

Example 3	UO_2 1.8%					UO_2 3.9% + 12 Gd pins				
	Variation (%)									
Type of effect	$\delta\Sigma_{a,1}$	$\delta\Sigma_{a,2}$	$\delta\nu\Sigma_{f,1}$	$\delta\nu\Sigma_{f,2}$	$\delta\Sigma_{s,1\to2}$	$\delta\Sigma_{a,1}$	$\delta\Sigma_{a,2}$	$\delta\nu\Sigma_{f,1}$	$\delta\nu\Sigma_{f,2}$	$\delta\Sigma_{s,1\to2}$
Spectral	0.0	−0.85	−0.44	−0.88	−0.92	0.082	0.80	0.32	0.84	0.98
Spatial	0.056	−0.21	0.072	−0.43	−0.056	−0.09	1.20	−0.005	0.084	0.038
Cross	−0.083	−0.030	−0.24	−0.019	0.08	0.12	0.51	0.13	0.036	−0.063
Global	−0.03	−1.09	−0.61	−1.33	−0.90	0.11	2.51	0.45	0.96	0.95

(d)

Example 4	UO_2 2.1%					MOX				
	Variation (%)									
Type of effect	$\delta\Sigma_{a,1}$	$\delta\Sigma_{a,2}$	$\delta\nu\Sigma_{f,1}$	$\delta\nu\Sigma_{f,2}$	$\delta\Sigma_{s,1\to2}$	$\delta\Sigma_{a,1}$	$\delta\Sigma_{a,2}$	$\delta\nu\Sigma_{f,1}$	$\delta\nu\Sigma_{f,2}$	$\delta\Sigma_{s,1\to2}$
Spectral	−0.43	−0.98	−0.41	−1.0	−3.43	0.92	0.47	0.34	0.50	2.46
Spatial	0.05	−0.30	0.066	−0.66	−0.035	−0.002	−0.37	0.033	−0.37	0.02
Cross	−0.15	0.11	−0.35	0.33	0.10	0.13	−0.41	0.17	−0.57	−0.095
Global	−0.53	−1.17	−0.70	−1.33	−3.36	1.06	−0.31	0.54	−0.44	2.39

reproduce to a high degree of accuracy the flux variation dip in the cells hosting absorbing elements (burnable-poison rods and control rods). In the 1-D approach, the flux change dip in these cells is smoothed out by the transverse integration and is therefore better fitted by the basis functions. When applying spatial and spectral rehomogenization sequentially, the overestimation of the spatial corrections in the thermal group may affect the accuracy of the global results.

The differences between the CPB-based and MSS-based approaches are small, with the former usually performing slightly better. An apparent superiority of the 2-D model over the 1-D model has not been observed. Except for the test case with gadolinium-bearing fuel pins in which the 2-D method is more accurate, the discrepancies between the two approaches are not significant. In general, the 1-D model overestimates the cross-section corrections to a lesser extent.

At the pin-by-pin level, on average better results are found when rehomogenization is applied. Nevertheless, the improvement in the heterogeneous flux and fission-power distributions is often not fully generalized, but limited to certain subregions of the fuel assemblies. Therefore, the accuracy of the computed fission power in the hot spots (that is, the fuel cells with the highest thermal load) is tied to their location within the fuel bundles.

We have observed that when 1-D or 2-D spatial rehomogenization is applied, the type of the transverse-leakage approximation does not affect the accuracy of the nodal calculation. An analysis on the complementarity of the various environmental corrections revealed that mixed energy-space effects cannot be neglected, especially in UO_2/MOX configurations.

The accuracy of the 2-D spatial rehomogenization might be improved by searching basis functions that better fit the intranodal flux spatial variation. Based on the satisfactory outcome of Proper Orthogonal Decomposition (POD) in the framework of spectral rehomogenization (Gamarino et al., 2018a; Gamarino et al., 2018b), this modal approach could be extended to the spatial problem as well. This strategy would allow the direct calculation of two-dimensional basis functions in the domain of space, thus discarding the separation of the directional and cross components of the modal expansion with one-dimensional modes.

In core configurations with strong heterogeneity in the axial direction (such as enrichment and gadolinium-concentration zoning in boiling water reactors), the 2-D rehomogenization in the x and y coordinates may be combined with the 1-D rehomogenization along the z axis. With this approach, modeling of axial heterogeneity could be improved while retaining coarse axial meshes for both 3-D assembly homogenization (Schneider et al., 2016), when applicable, and the on-line nodal calculation.

Acknowledgment

This work was supported by the Framatome Ph.D. program.

References

Bahadir, T., Lindahl, S., 2009. Studsvik's next generation nodal code SIMULATE-5. In: Proc. of Advances in Nuclear Fuel Management IV (ANFM 2009), Hilton Head Island, South Carolina, USA.

Bahadir, T., Lindahl, S., Palmtag, S.P., 2005. SIMULATE-4 multigroup nodal code with microscopic depletion model. In: Proc. of Mathematics and Computation, Supercomputing, Reactor Physics and Nuclear and Biological Applications (M&C 2005), Avignon, France.

Böer, R., Finnemann, H., 1992. Fast analytical flux reconstruction method for nodal space-time nuclear reactor analysis. Ann. Nucl. Energy 19 (10–12), 617–628.

Chang, M.H., Moon, K.S., Noh, J.M., Kim, S.H., 1989. A nodal expansion method with spatially coupled effects incorporated into the transverse leakage approximation. Nucl. Sci. Eng. 103 (4), 343–350.

Clarno, K.T., Adams, M.L., 2005. Capturing the effects of unlike neighbors in single-assembly calculations. Nucl. Sci. Eng. 149 (2), 182–196.

Dall'Osso, A., 2002. Reducing rod cusping effect in nodal expansion method calculations. In: Proceedings of the International Conference on the New Frontiers of Nuclear Technology: Reactor Physics, Safety and High-Performance Computing, PHYSOR 2002, Seoul, Korea.

Dall'Osso, A., 2014. Spatial rehomogenization of cross sections and discontinuity factors for nodal calculations. In: Proc. of Int. Conf. PHYSOR 2014, Kyoto, Japan.

Forslund, P., Müller, E., Lindahl, S., 2001. Investigation of intranodal depletion effects. Ann. Nucl. Energy 28 (3), 225–250.

Gamarino, M., Dall'Osso, A., Lathouwers, D., Kloosterman, J.L., 2018b. A neutron-leakage spectrum model for on-the-fly rehomogenization of nodal cross sections. Ann. Nucl. Energy 116, 257–279.

Gamarino, M., Dall'Osso, A., Lathouwers, D., Kloosterman, J.L., 2018a. Rehomogenization of nodal cross sections via modal synthesis of neutron spectrum changes. Nucl. Sci. Eng. 190 (1), 1–30.

Groenewald, S.A., Prinsloo, R.H., Zamonsky, O.M., 2017. Practical semi-heterogeneous method in nodal core analysis. In: Proc. of Int. Conf. on Mathematics and Computational Methods Applied to Nuclear Science and Engineering (M&C 2017), Jeju, Korea.

Guillo, M., Calloo, A., Couyras, D., Févotte, F., Brosselard, C., Bouriquet, B., Dubois, A., Girardi, E., Hoareau, F., Fliscounakis, M., Leroyer, H., Noblat, E., Pora, Y., Plagne, L., Ponçot, A., Schwartz, N., 2017. COCAGNE: EDF new neutronic core code for ANDROMÈDE calculation chain. In: Proc. of Int. Conf. on Mathematics and Computational Methods Applied to Nuclear Science and Engineering (M&C 2017), Jeju, Korea.

Hebert, A., 2009. Applied Reactor Physics. Presses Internationales Polytechnique.

Joo, H.G., Yoon, J.I., Baek, S.G., 2009. Multigroup pin power reconstruction with two-dimensional source expansion and corner flux discontinuity. Ann. Nucl. Energy 36 (1), 85–97.

Khoshahval, F., Zolfaghari, A., Minuchehr, H., 2014. Effect of including corner point fluxes on the pin power reconstruction using nodal point flux scheme. Ann. Nucl. Energy 69, 25–36.

Kim, W., Heo, W., Kim, Y., 2017. Improvement of nodal accuracy by using albedo-corrected parameterized equivalence constants. Nucl. Sci. Eng. 188 (3), 207–245.

Lawrence, R.D., 1986. Progress in nodal methods for the solution of the neutron diffusion and transport equations. Prog. Nucl. Energy 17 (3), 271–301.

Martinolli, E., Carter, T.C., Clement, F., Demy, P.M., Leclere, M., Magat, P., Marquis, A., Marotte, V., Schneider, M., Villatte, L., et al., 2010. APOLLO2-A – AREVA's new generation lattice physics code: methodology and validation. In: Proc. of Int. Conf. PHYSOR 2010, Pittsburgh, Pennsylvania, USA.

McKinley, M.S., Rahnema, F., 2000. High-order boundary condition perturbation theory for the diffusion approximation. Nucl. Sci. Eng. 136 (1), 15–33.

Palmtag, S.P., 1997. Advanced Nodal Methods for MOX Fuel Analysis (Ph.D. thesis). Massachusetts Institute of Technology.

Palmtag, S.P., Smith, K.S., 1998. Two-group spectral corrections for MOX calculations. In: Proc. of the Int. Conf. on the Physics of Nuclear Science and Technology, vol. 1, Long Island, New York, USA. p. 3.

Prinsloo, R.H., Tomašević, D.I., Moraal, H., 2014. A practical implementation of the higher-order transverse-integrated nodal diffusion method. Ann. Nucl. Energy 68, 70–88.

Rahnema, F., McKinley, M.S., 2002. High-order cross-section homogenization method. Ann. Nucl. Energy 29 (7), 875–899.

Rahnema, F., Nichita, E.M., 1997. Leakage corrected spatial (assembly) homogenization technique. Ann. Nucl. Energy 24 (6), 477–488.

Rempe, K.R., Smith, K.S., Henry, A.F., 1989. SIMULATE-3 pin power reconstruction: methodology and benchmarking. Nucl. Sci. Eng. 103 (4), 334–342.

Sanchez, R., 2009. Assembly homogenization techniques for core calculations. Prog. Nucl. Energy 51 (1), 14–31.

Schneider, D., Dolci, F., Gabriel, F., Palau, J.M., Guillo, M., Pothet, B., Archier, P., Ammar, K., Auffret, F., Baron, R., et al., 2016. APOLLO3: CEA/DEN deterministic multi-purpose code for reactor physics analysis. In: Proc. of Int. Conf. PHYSOR 2016, Sun Valley, Idaho, USA.

Shatilla, Y.A., Chao, Y.A., Tahara, Y., 1996. Theory of Westinghouse advanced nodal code for MOX applications. Trans. Am. Nucl. Soc. 75.

Smith, K.S., 1986. Assembly homogenization techniques for Light Water Reactor analysis. Prog. Nucl. Energy 17 (3), 303–335.

Smith, K.S., 1994. Practical and efficient iterative method for LWR fuel assembly homogenization. Trans. Am. Nucl. Soc. 71.

Stacey, W.M., 2007. Nuclear Reactor Physics. John Wiley & Sons.

Wagner, M.R., Koebke, K., Winter, H.-J., 1981. A non-linear extension of the nodal expansion method. In: Proc. of Int. Conf. in Advances in Mathematical Methods for the Solution of Engineering Problems, vol. 2, Munich, Germany. p. 43.